Imaging [CI] around HD 131835: reinterpreting young debris discs with protoplanetary disc levels of CO gas as shielded secondary discs

Quentin Kral, Sebastian Marino, Mark Wyatt, Mihkel Kama, Luca Matra

Monthly Notices of the ROYAL ASTRONOMICAL SOCIETY

MNRAS **489,** 3670–3691 (2019) doi:10.1093/mnras/sty2923
Advance Access publication 2018 November 22

Imaging [CI] around HD 131835: reinterpreting young debris discs with protoplanetary disc levels of CO gas as shielded secondary discs

Quentin Kral [1,2★] Sebastian Marino [1] Mark C. Wyatt,[1] Mihkel Kama,[1] and Luca Matrà[3]

[1] *Institute of Astronomy, University of Cambridge, Madingley Road, Cambridge CB3 0HA, UK*
[2] *LESIA, Observatoire de Paris, Université PSL, CNRS, Sorbonne Université, Univ. Paris Diderot, Sorbonne Paris Cité, 5 place Jules Janssen, F-92195 Meudon, France*
[3] *Harvard-Smithsonian Center for Astrophysics, 60 Garden Street, Cambridge, MA 02138, USA*

Accepted 2018 October 22. Received 2018 September 28; in original form 2018 August 2

ABSTRACT

Despite being >10 Myr, there are ∼10 debris discs with as much CO gas as in protoplanetary discs. Such discs have been assumed to be 'hybrid', i.e. with secondary dust but primordial gas. Here, we show that both the dust and gas in such systems could instead be secondary, with the high CO content caused by accumulation of neutral carbon (C^0) that shields CO from photodissociating; i.e. these could be 'shielded secondary discs'. New ALMA observations are presented of HD131835 that detect $\sim 3 \times 10^{-3}$ $M_\oplus$ of C^0, the majority 40–200 au from the star, in sufficient quantity to shield the previously detected CO. A simple semi-analytic model for the evolution of CO, C, and O originating in a volatile-rich planetesimal belt shows how CO shielding becomes important when the viscous evolution is slow (low α parameter) and/or the CO production rate is high. Shielding by C^0 may also cause the CO content to reach levels at which CO self-shields, and the gas disc may become massive enough to affect the dust evolution. Application to the HD 131835 observations shows these can be explained if $\alpha \sim 10^{-3}$; an inner cavity in C^0 and CO may also mean the system has yet to reach steady state. Application to other debris discs with high CO content finds general agreement for $\alpha = 10^{-3}$ to 0.1. The shielded secondary nature of these gas discs can be tested by searching for C^0, as well as CN, N_2, and CH^+, which are also expected to be shielded by C^0.

Key words: accretion, accretion discs – circumstellar matter – planetary systems.

1 INTRODUCTION

Gas is now detected routinely around main-sequence stars that possess planetesimal belts similar to the Kuiper belt. On the order of 20 systems show the presence of gas (e.g. Kóspál et al. 2013; Greaves et al. 2016; Lieman-Sifry et al. 2016; Hughes et al. 2017; Moór et al. 2017) and this number will soon increase, mostly thanks to upcoming surveys with ALMA. Most of these systems have CO detected in emission (often colocated with the planetesimal belt) and for a handful of them ionized carbon and oxygen were detected with Herschel (e.g. Riviere-Marichalar et al. 2012, 2014; Brandeker et al. 2016; Kral, Clarke & Wyatt 2017b). Neutral carbon (C^0) has been predicted to be a good tracer of gas in these systems (Kral et al. 2017c) and has now been detected around 49 Ceti and β Pic (Higuchi et al. 2017; Cataldi et al. 2018).

The origin of the gas around these main-sequence stars is still debated for some systems (because of their youth that can be close to 10 Myr or older), i.e. whether the gas is a remnant of the protoplanetary disc (called primordial hereafter) or released at a later stage (i.e. secondary). However, for at least three systems (HD 181327, β Pic, and Fomalhaut) the CO mass detected is so low that it cannot be primordial as neither CO nor H_2 (even assuming an extreme CO-to-H_2 ratio of 10^{-6}) could shield CO from photodissociating owing to the UV radiation from the interstellar radiation field (Marino et al. 2016; Matrà et al. 2017a,b). We also note that the presence of gas around the 440-Myr-old Fomalhaut star (Matrà et al. 2017b) and possibly around the 1-Gyr-old η Corvi (Marino et al. 2017) leaves no doubt concerning the secondary origin of the gas there.

Kral et al. (2017c) show that a second-generation model where the gas is released from volatile-rich planetesimals colliding in the belts (e.g. Zuckerman & Song 2012) can explain most of the detections and non-detections so far (for >10 Myr systems), assuming planetesimals with a composition similar to Solar System comets, reinforcing the idea that most of the observed gas is secondary. However, the high-mass gas discs, called hybrid discs by Kóspál et al. (2013) because of their high, assumed primordial,

★ E-mail: quentin.kral@obspm.fr

CO content but low debris-disc like secondary dust mass, could not be explained with this model and were deemed to be of primordial origin.

We consider in this paper whether these high gas mass systems can actually also be explained as being of secondary origin due to an ingredient that was missing in the previous model: *the C^0 shielding effect*.[1] This effect is now accounted for in a new model presented in this paper and applied to a new [CI] ALMA detection towards HD 131835 also presented in this paper.

HD 131835 is a 15–16-Myr-old (Mamajek, Meyer & Liebert 2002; Pecaut, Mamajek & Bubar 2012) A-type star located at a distance[2] of 145 ± 9 pc (Gaia Collaboration 2016a,b) that is probably a member of the Upper Centaurus Lupus moving group (a subgroup of the Sco-Cen association, Rizzuto, Ireland & Robertson 2011). An infrared (IR) excess around this star has first been reported by Moór et al. (2006), establishing the presence of a bright debris disc. The disc was first resolved in mid-infrared using T-ReCS from which it could be deduced that multiple disc components were needed to fit the data (Hung et al. 2015b). More recently, SPHERE observations in the near-IR led to the detection of a series of narrow concentric rings (Feldt et al. 2017). Such concentric rings may be explained by the presence of large quantities of gas (e.g. Takeuchi & Artymowicz 2001; Lyra & Kuchner 2013; Richert, Lyra & Kuchner 2018).

CO gas has recently been discovered around HD 131835 using APEX (Moór et al. 2015) and has been followed-up with ALMA from which the total CO mass derived (using an optically thin line) is ∼0.04 $M_\oplus$ (after correction for the new *Gaia* distance, Moór et al. 2017). This CO mass is of the same order of magnitude as for the famous TW Hya protoplanetary disc (Favre et al. 2013), leading to the possibility that the disc is primordial.

From the new [CI] observations we present in this paper, we show that the observed gas in the so-called 'hybrid' disc around HD 131835 (or HIP 73145) is compatible with being a shielded debris disc, i.e. a massive gas disc of secondary origin. Furthermore, we conclude that some or all of the so-called hybrid discs might not be hybrid after all but just entirely second generation, both in their gas and dust content. For this reason, from now on we will call these discs: *shielded discs* rather than hybrid. To make the distinction easier, we call the low CO mass systems of secondary origin 'unshielded' and the high CO mass systems 'shielded'. This has important consequences for our understanding of the fate of protoplanetary discs that, if true, would not survive as long as previously thought and would indicate that massive secondary gaseous debris discs can start early, while planet formation may still be on-going.

In Section 2, we start by introducing the new concept of shielded discs that can explain massive CO gas discs as being of secondary origin rather than hybrid. In Section 3, we present new continuum observations of HD 131835 with ALMA and a fit of the data with a dust model. We then carry on by showing the first neutral carbon detections of HD 131835 with ALMA and a fit of the data set with several gas models in Section 4. In Section 5, we discuss the implications of this new [CI] detection and how it backs up the shielded disc scenario. We first describe a self-consistent physical model that can explain the observed high CO mass together with the new [CI] detection assuming a secondary origin of the gas. We then constrain the viscosity of the observed gas disc (using an α parametrization), derive the expected composition of the (exo)planetesimals in this system and discuss the dust/gas interactions that may happen. Finally, before concluding, we discuss the possibility that all hybrid discs discovered so far (possibly up to nine systems) are in fact shielded discs, i.e. not hybrid, and we derive some constraints on their gas disc viscosity (α) and predict their content in C^0 that is within reach of ALMA.

2 SECONDARY GAS DISCS AND INTRODUCTION TO THE NEW CATEGORY OF SHIELDED DISCS

2.1 Standard evolution of low-mass unshielded secondary gas discs

In a secondary gas production scenario, gas is released in the planetesimal belt, while volatile-rich bodies collide with each other. CO and water are expected to be the major constituents of comets (assuming Solar System-like compositions), and will possibly dominate the release (note that this depends on the exact mechanism that releases this gas, see Matrà et al. 2018a). In the standard secondary approach presented in Kral et al. (2016, 2017c), CO and water photodissociate very quickly because of the UV radiation from the interstellar radiation field (i.e. typically in about 100 yr) because there is not enough CO to self-shield nor enough H_2 that could increase the CO or water lifetime. Carbon, oxygen, and hydrogen are thus created very quickly through photodissociation, which builds an atomic gas disc that viscously spreads. In our model, the viscosity is parametrized with an α parameter (as in Xie, Brandeker & Wu 2013), which has been inferred to be high in the β Pic gas disc, i.e. $\alpha > 0.1$, leading to a viscous time-scale $t_\nu <$ 0.5 Myr (Kral et al. 2016) as the viscous evolution time-scale at R_0, $t_\nu(R_0)$ is given by $R_0^2\Omega/(\alpha c_s^2)$, where the orbital frequency Ω and the sound speed c_s are both estimated at R_0 (taken to be 85 au for β Pic). However, in systems in which the carbon ionization fraction is smaller, and therefore the magnetorotational instability is less effective (Kral & Latter 2016), the resulting α could be much smaller (e.g. 10^{-3}), resulting in a much longer viscous time-scale.

To illustrate the implication of a change in α for the evolution of the disc, Fig. 1 shows the temporal evolution of a gas disc with a steady input of gas at a rate of $\dot{M}_{\rm CO} = 10^{-2}$ $M_\oplus$ Myr^{-1} at $R_0 = 90$ au, which is converted to a C^0 input rate by assuming an ionization fraction f of 0.1. The evolution is worked out semi-analytically using solutions found by Tanaka (2011), where we assumed the temperature to be $\propto R^{-\beta}$, with $\beta = 1/2$. For a β Pic-like system with $\alpha = 0.5$ (solid black lines), the steady state is reached after only a few Myr (i.e. longer time-scale lines all coincide on the steady state uppermost solid black line). For a model in which $\alpha = 10^{-3}$ (green dashed lines), the steady state is not yet reached after 15 Myr (last epoch shown in the figure). In this case, the evolution is 500 times slower and much more carbon can accumulate in the system, reaching number densities n_{C^0} of $\sim 10^4$ cm^{-3} at R_0 after 15 Myr. We also plot the predicted analytical steady state values

[1] We note that C^0 shielding was taken into account in the numerical model by Kral et al. (2016) studying β Pic, but only for its impact on ionization fraction and temperature, but not for the CO content as the C^0 mass for β Pic is not large enough to shield CO. Matrà et al. (2017a) showed later that indeed in β Pic, the shielded CO photodissociation rate due to C^0 is 0.96 of the unshielded one, i.e. not important.

[2] We note that the *Hipparcos* distance assumed in previous studies was $122.75^{+16.2}_{-12.8}$, which is consistent within error bars with the GAIA DR1 value, but the median ratio is 1.18 (van Leeuwen 2007), which can affect some earlier derived model values such as dust or gas masses, stellar luminosities, ... In particular, distances from previous studies should be multiplied by 1.18 before comparing to our study.

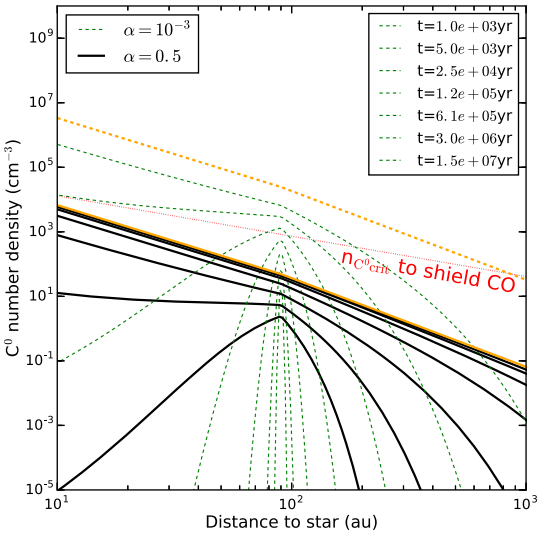

Figure 1. Evolution of the C^0 number density as a function of radius and for several time-steps (from 10^3 yr to 15 Myr) for carbon inputted at a steady rate at 90 au. The carbon gas is assumed to spread viscously with time with a time-scale that depends on the viscosity parametrized by α. We show a fast evolution with $\alpha = 0.5$ (black solid lines) and a slower evolution with $\alpha = 10^{-3}$ (green dashed lines). The high-α disc reaches a steady state after a few Myr while the low-α disc is still evolving after 15 Myr. The red dotted line shows the critical C^0 density above which C^0 starts shielding CO from photodissociation. For the low-α case, we note that the C^0 density is high enough to extend the CO lifetime and CO will accumulate owing to C^0 shielding, which will lead to a shielded disc as defined in Section 2. To compute the C^0 input rate, we assumed $\dot{M}_{CO} = 10^{-2}$ M$_\oplus$ and an ionization fraction of 0.1. The orange lines show the steady state number density for $\alpha = 0.5$ (solid) and 10^{-3} (dashed) based on equation (1).

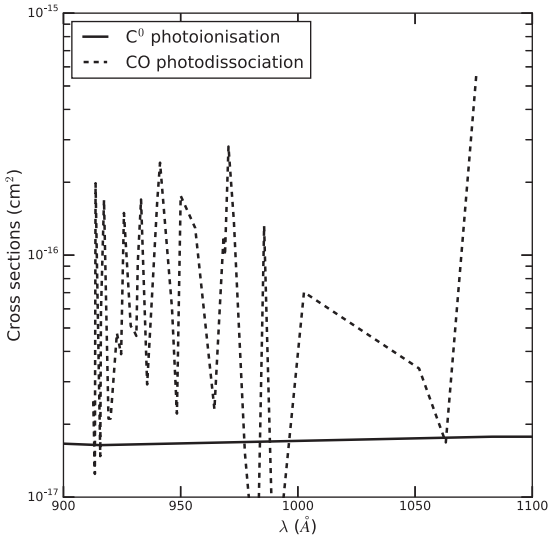

Figure 2. C^0 photoionization (solid, van Dishoeck 1988) and CO photodissociation (dashed, Visser, van Dishoeck & Black 2009) cross-sections between 900 and 1100 Å. The same energetic photons that can photodissociate CO can photoionize neutral carbon.

that we find to be (updating the solutions for the case $\beta = 1/2$ by Lynden-Bell & Pringle 1974, to our case of a steady input)

$$\Sigma(R) = \frac{\dot{M}}{3\pi\nu_0} \begin{cases} \left(\frac{R}{R_0}\right)^{\beta-3/2} & \text{for } R < R_0 \\ \left(\frac{R}{R_0}\right)^{\beta-2} & \text{for } R > R_0 \end{cases}, \quad (1)$$

where $\nu_0 = \alpha c_s^2(R_0)/\Omega(R_0)$ is the viscosity at R_0, the temperature $T \propto R^{-\beta}$, and $\dot{M}$ is the input rate (for C^0, $\dot{M} = 12/28\dot{M}_{CO}(1-f)$). Metzger, Rafikov & Bochkarev (2012) also derive this formula (in their appendices) and show that it is valid not only for $\beta = 1/2$ but for all values of β. Therefore, at steady state the number density scales as $R^{3\beta/2-3}$ for $R < R_0$ and as $R^{3\beta/2-7/2}$ for $R > R_0$ as shown by the orange analytical steady state profiles plotted in Fig. 1.

2.2 Shielded discs

The shielded disc case happens when the C^0 density becomes high enough that C^0 gets optically thick to UV radiation. The C^0 photoionization cross-section is roughly constant (see Fig. 2) and equal to $\sigma_i = 1.6 \times 10^{-17}$ cm^2 (van Dishoeck 1988) from 900 Å (i.e. close to the Lyman break at 13.6 eV) to ∼1100 Å (i.e. 11.26 eV, which is the ionization potential of carbon). Fig. 2 shows that the photodissociation cross-sections of CO (Visser et al. 2009) are affected by the same photons (i.e. from 910 to 1075 Å) that can ionize carbon. Calculating the C^0 column density N_{C^0} from n_{C^0} in Fig. 1 for the $\alpha = 10^{-3}$ model at 15 Myr, we find that for a UV photon from the interstellar radiation field (IRF, that dominates the UV flux at the typical distances of typical planetesimal belts R_0, Matrà et al. 2018b) travelling in the vertical direction, C^0 is indeed optically thick to UV radiation (we note that it is much more optically thick in the radial direction and the star UV field is thus not expected to contribute to CO photodissociation in these shielded discs). This means that if C^0 is blocking the UV photons, CO will photodissociate on longer time-scales. Indeed, Rollins & Rawlings (2012) compute that the CO photodissociation time-scale (in yr) in the presence of C^0 is

$$t_{CO} = 120\,\text{yr} \times \exp(\sigma_i N_{C^0}), \quad (2)$$

where 120 yr is the photodissociation time-scale without shielding, i.e. when only the IRF is taken into account. This shows that shielding of CO by C^0 starts happening for $N_{C^0} \gtrsim 10^{16}$ cm^{-2}. We note that we considered shielding in the vertical direction and shielding in the radial direction is expected to be much higher because of the greater column density towards the star.

Fig. 3 shows how much C^0 mass is needed for the CO photodissociation time-scale to depart from 120 yr. Here, we also assume that $R_0 = 90$ au and a width of 70 au so that $M_{C^0} = N_{C^0} 2\pi R \Delta R \mu_c m_H$, where μ_c is the mean molecular weight of carbon. For a C^0 mass of $\sim 10^{-3}$ M$_\oplus$, t_{CO} is 200 yr and as the evolution follows a very steep exponential profile, for $M_{C^0} = 1.2 \times 10^{-2}$ M$_\oplus$, then $t_{CO} = 10^5$ yr. For the latter case, this means that the CO mass expected from second-generation models such as described in Kral et al. (2017c) can be more than $t_{CO}/120 \sim 10^3$ times larger than previously thought and one can accumulate CO masses of the order of the mass content found in a protoplanetary disc such as TW Hydra (Favre et al. 2013).

Therefore, the high CO mass content (∼0.04 M$_\oplus$) found by Moór et al. (2017) for HD 131835 could be compatible with a gas production of secondary origin for high enough C^0 masses in the disc as summarized by the sketch presented in Fig. 4. This will be checked in more detail in Section 5 presenting some new modelling of this C^0 shielding effect but first let us check the spatial distribution of the dust (Section 3) and gas from new ALMA observations and whether there is enough C^0 observed to produce this shielding (Section 4).

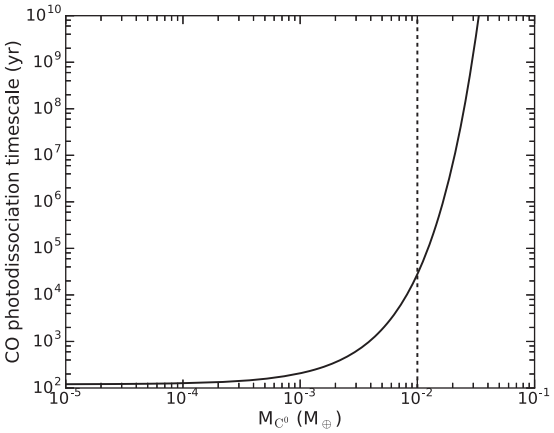

Figure 3. CO photodissociation time-scale (in yr) as a function of the C^0 mass (M_{C^0} in $M_\oplus$) in the gas disc. This time-scale depends exponentially on C^0 mass and a small amount of C^0 can create a large accumulation of CO that is then very hard to photodissociate because the UV photons that could potentially do that are mostly absorbed by C^0 beforehand (see also Fig. 2). We assumed a disc located at 90 au of width 70 au. The dashed line is for a C^0 mass of 10^{-2} $M_\oplus$ for which the photodissociation time-scale is already more than 100 times longer than when just assuming the interstellar radiation field (∼120 yr).

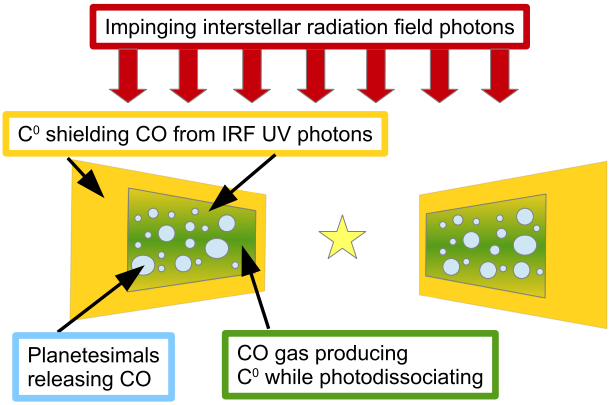

Figure 4. Sketch of the secondary gas model, where (1) gas is released from the solid bodies in a Kuiper-belt like disc, (2) C^0 is produced by photodissociation of CO and viscously spread towards the inner region, (3) the C^0 gas disc can become massive enough that it absorbs most photons from the interstellar radiation field that could have photodissociated CO so that CO accumulates and can reach protoplanetary CO mass level. Note that carbon is also present in the green region and that it is more extended outwards than CO.

3 ALMA CONTINUUM OBSERVATION OF HD 131835

HD 131835 was observed by ALMA in band 8 in 2017 March 22 as part of the cycle 4 project 2016.1.0.01253. The observations were carried out using 42 antennas with baselines ranging from 15 to 160 m. The total observing time on source (excluding overheads) was 14.1 min and the mean PWV was 0.57 mm.

Out of the four spectral windows provided by the ALMA correlator, three focused on observing the dust continuum with 128 channels centred at 480.201, 482.159, and 494.201 GHz (bandwidth of 2 GHz). The fourth spectral window targeted the CI ($^3P_0$-$^3P_1$) transition at 492.160651 GHz (i.e. a rest wavelength of 609.135 μm) with a higher spectral resolution of 488.281 kHz (0.297 km s^{-1} at

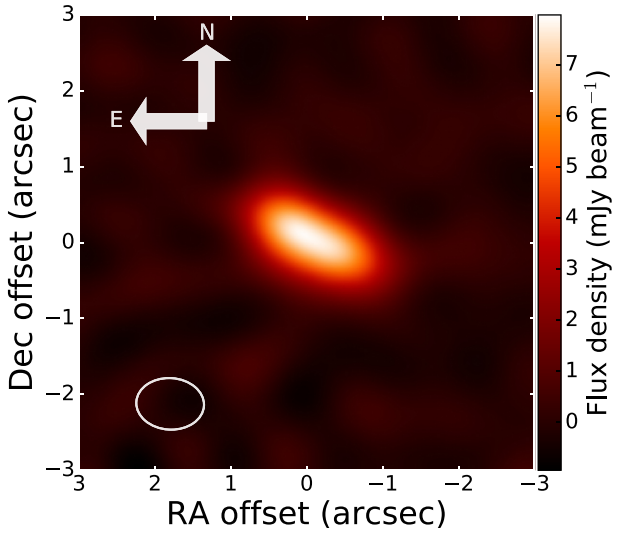

Figure 5. ALMA dust continuum map of HD 131835 at 487 GHz (band 8). The image is Briggs-weighted (with robust = 0.5). The ellipse shows the beam of 0.89 × 0.68 arcsec and the North and East directions are indicated by the two arrows. The *x*- and *y*-axes indicate the offset from the stellar position in RA and Dec (in arcsec).

the rest frequency of the line) over 3840 channels (i.e. a bandwidth of 1.875 GHz) centred at 492.201 GHz. Titan was used as a flux calibrator, while J1427-4206 and J1454-3747 were used as bandpass and phase calibrator, respectively. We used the pipeline provided by ALMA to apply calibrations.

3.1 Dust continuum observations

Fig. 5 shows the ALMA dust continuum map of HD 131835 at ∼487 GHz (i.e. 616 μm). All the analysis that follows uses the visibilities but we show the image to introduce the data to the reader and provide some first qualitative idea of the observation. We deconvolved the image using the CLEAN algorithm and Briggs weighting with a robust parameter of 0.5. This yields a synthesized beam of 0.89 × 0.68 arcsec (i.e. ∼129 × 97 au, assuming a distance of 145 pc from Earth). The peak signal-to-noise ratio (S/N) in the image is ∼32. The image rms around the disc is $\sigma = 250\,\mu$Jy beam^{-1}. The total flux in the Briggs-weighted image is 17.9 ± 2.1 mJy, where the error comes from the image noise and flux calibration uncertainties (∼10 per cent) added in quadrature.

The bulk of the emission is within 1 arcsec (i.e. ∼145 au) and appears consistent with a highly inclined axisymmetric disc as found from previous resolved observations of the disc at different wavelengths (e.g. Hung et al. 2015b; Feldt et al. 2017). The disc parameters such as inclination, PA, and disc mass are derived in the next Section 3.2 using an MCMC approach to fit a dust disc model to the observed visibilities.

3.2 Fit of the continuum data

We now compare the ALMA visibilities (V_{obs}) for the dust continuum to an axisymmetric dust model. The disc model is parametrized as a ring of radius R_0 with a Gaussian radial profile of full width at half-maximum (FWHM) W_{ring}. We also assume a Gaussian vertical profile of aspect ratio $h = H/R$ (H being the scale height) such that

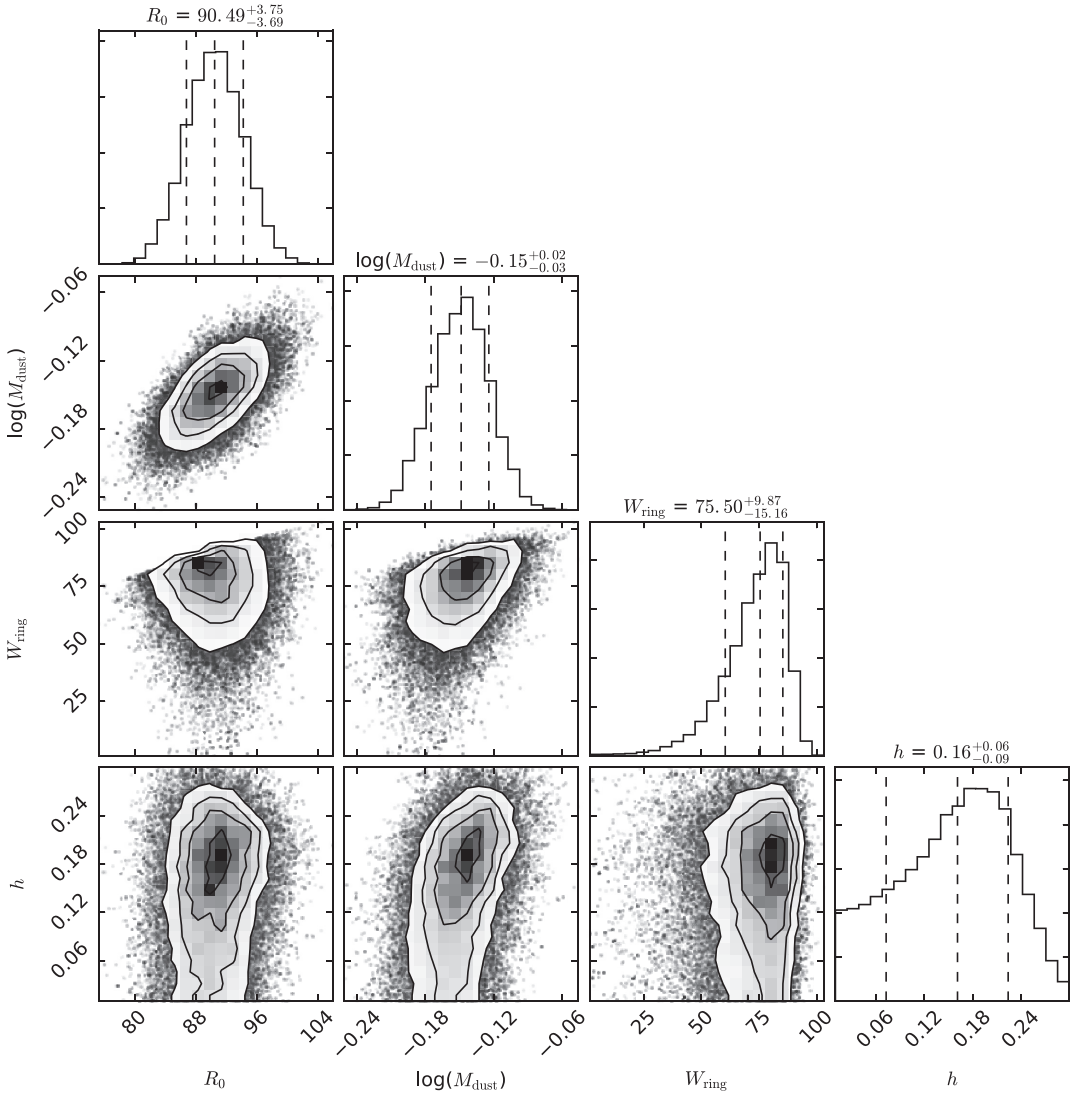

Figure 6. Posterior distribution of the dust continuum model for R_0, $M_{\rm dust}$, $W_{\rm ring}$, h (see Section 3.2). The marginalized distributions are presented in the diagonal. The vertical dashed lines represent the 16th, 50th, and 84th percentiles.

the dust density distribution is

$$\rho_d(R, Z) = \rho_0 \exp\left(-\frac{(R - R_0)^2}{2\sigma_d^2}\right) \exp\left(-\frac{Z^2}{2H^2}\right), \quad (3)$$

where ρ_0 is the density at R_0 in the mid-plane and $\sigma_d = W_{\rm ring}/(2\sqrt{2\log 2})$. We then use the line radiative transfer code RADMC-3D (Dullemond et al. 2012) to compute images for a given dust model (as in Marino et al. 2016) and GALARIO (Tazzari, Beaujean & Testi 2018) to convert them into model visibilities ($V_{\rm mod}$) that can be compared to the data in an MCMC fashion. For the dust optical properties, we assume an astrosilicate composition with a density of 2.7 g cm^{-3} (Draine 2003) and use a mass-weighted mean opacity of $\kappa = 2.5$ cm^{2}g^{-1} at 610 μm that is computed using the Mie theory code from Bohren & Huffman (1983). The size distribution is assumed to be between a minimum size of 2.5 μm (corresponding to the blow out size derived from Burns, Lamy & Soter 1979) and a maximum size of 1 cm (larger grains do not participate to flux observed in band 8) with a power-law index of −3.5, which is similar to what is predicted analytically for debris discs (Dohnanyi 1969) or from numerical simulations (e.g. Krivov, öhne & Sremvcević 2006; Thébault & Augereau 2007; Kral, Thébault & Charnoz 2013).

Therefore, the free parameters that are left, which are fitted in our model, are: R_0, $W_{\rm ring}$, h, inclination (i), PA and $M_{\rm dust}$, where the latter is the total dust mass up to 1 cm bodies. We also allow an offset in RA (offset x) and Dec (offset y) to account for astrometric uncertainties in the ALMA data. We use a Bayesian MCMC approach to constrain the eight free parameters of the model. We sample the parameter space by using the emcee module (see Goodman & Weare 2010; Foreman-Mackey et al. 2013, for the details of the method). We assume that the priors are uniform and the posterior distribution is then given by the product between the prior distribution function and the likelihood function, which is assumed to be $\propto \exp(-\chi^2/2)$, with $\chi^2 = \sum(V_{\rm obs} - V_{\rm mod})^2/\sigma_V^2$ (σ_V being the variance of the data). We ran the MCMC with 100 walkers and for 1200 steps after the burn-in period.

The posterior distributions obtained are shown in Fig. 6 for the four most important parameters and we summarize all the best-fitting parameters in Table 1. The inclination ($\sim$ 79 deg) and PA ($\sim$ 59 deg) found by our MCMC calculations are consistent with other

Table 1. Table describing the best-fitting parameters of the dust modelling using an MCMC method (see Section 3.2). We list the median ± uncertainties, which are based on the 16th and 84th percentiles of the marginalized distributions.

Parameters	Best-fitting values
R_0 (au)	$90.5^{+3.8}_{-3.7}$
$M_{\rm dust}$ ($M_\oplus$)	$0.71^{+0.03}_{-0.05}$
$W_{\rm ring}$ (au)	$75.5^{+9.9}_{-15.2}$
h	$0.16^{+0.06}_{-0.09}$
i (deg)	$79.4^{+6.8}_{-5.2}$
PA (deg)	$59^{+2}_{-1.9}$
RA offset ($''$)	$-0.09^{+0.02}_{-0.02}$
Dec offset ($''$)	$-0.07^{+0.02}_{-0.02}$

studies (Hung et al. 2015b; Moór et al. 2015). The offsets in x and y are also consistent with the ALMA astrometric uncertainties (∼0.1 arcsec, see ALMA technical handbook[3]).

The disc radius R_0 is constrained to be around 90 au. The width (FWHM) of the ring that we derive from our model is ∼76 au (0.52 arcsec), which is however smaller than the beam size and thus must be understood as having large uncertainties. A strict upper limit of 95 au can, however, be derived at the 99.7 per cent level. From these results, the bulk of the parent belt would be between ∼50 and 140 au. Hung et al. (2015a) observed HD 131835 with T-ReCS in the mid-IR and show that the best fit is for a continuous disc extending from ∼40 to 350 au plus two rings at ∼124 and ∼260 au (after correcting for the new *Gaia* distance). The two rings may be made of very small micron-sized grains (see discussion) and are thus not expected to be seen in the ALMA image. The continuous disc observed with T-ReCS extends farther away than ALMA is sensitive to, because mid-IR observations are sensitive to smaller grains that have very eccentric orbits (owing to radiation pressure) and create an extended halo (while ALMA is not). Feldt et al. (2017) observed the disc with SPHERE and detected the presence of three concentric rings at ∼116, 78, and 46 au. They also published an ALMA band 6 continuum image that looks similar to Fig. 5 with a lower resolution and also find that the ALMA emission is more compact than at smaller wavelengths.

The dust mass derived from our model is ∼0.7 $M_\oplus$. This is consistent with the fit by Moór et al. (2015), who found $0.65 \pm 0.25\ M_\oplus$ (after correcting for the new *Gaia* distance). These estimates depend on the assumptions made for the composition and size distribution of the bodies whereas the structure does not. The aspect ratio estimation h is limited because of the relatively low resolution of the observation but we find a best fit of 0.16 and that it is smaller than 0.29 at 99.7 per cent confidence level. It, however, may be much smaller than 0.16 as observed with SPHERE in the near-IR (Feldt et al. 2017).

Finally, we show the best-fitting model along with the data in the visibility plane (azimuthally averaged assuming $i = 79.4$ deg and PA = 59 deg) in Fig. 7 (in a similar way as in Hughes et al. 2011). We also subtracted our best-fitting model from the data in the image plane and checked that the remaining residuals were all within the expected noise level.

[3]https://almascience.eso.org/documents-and-tools/cycle6/alma-technical-handbook

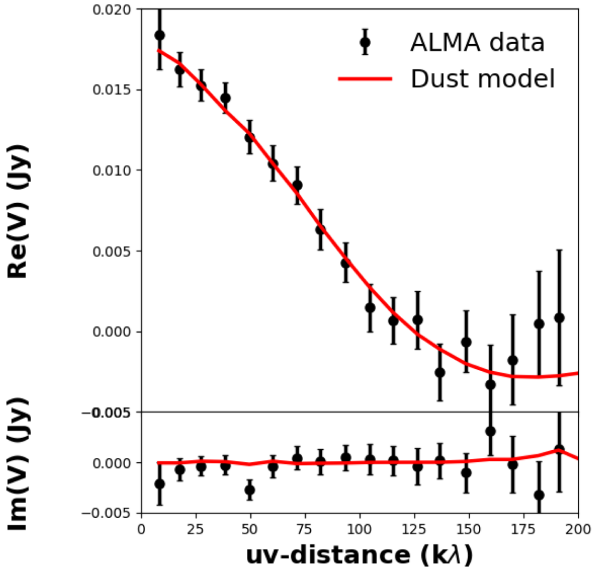

Figure 7. Real part (top) and imaginary part (bottom) of the continuum data visibilities (black dots with errors bars) along with the best-fitting model (overplotted red line) described in Section 3.2 and whose parameters are given in Table 1. The uv-distances are given in units of observing wavelength and visibilities in Jansky.

4 ALMA [CI] OBSERVATION OF HD 131835

4.1 C^0 gas detection

To obtain the CI $^3P_0$-$^3P_1$ (at a rest wavelength of 609.135 μm) emission map, we first subtract the continuum emission directly from the visibilities (with the task UVCONTSUB in CASA) using only channels where no [CI] emission is expected. Fig. 8 shows the moment-0 (i.e. spectrally integrated) [CI] detection around HD 131835. Once again, we show the image to familiarize the reader with the qualitative features of the observation but we only use the observed visibilities in the rest of the paper when it comes to fitting models (see Section 4.2). We used the CLEAN algorithm to deconvolve the image using Briggs (with robust = 0.5). The synthesized beam (shown as an ellipse in Fig. 8) has a size of 0.89 × 0.63 arcsec. We find that the 1σ noise level near the disc in the moment-0 image is 66 mJy km s^{-1} beam^{-1} so that the peak S/N is 18. The total integrated flux is 2.8 ± 0.4 Jy km s^{-1}, which was measured by integrating over a region large enough that it contains all disc emission but small enough that it is not affected by noise contamination (an ellipse of size 3 × 2.5 arcsec). The error takes account of the noise in the image and flux calibration uncertainties that were added in quadrature.

In Fig. 9, we show the radial profile of the [CI] emission along the mid-plane. The flux is integrated vertically within ±100 au from the rotated moment-0 image. The 2σ integrated noise is shown as a blue shaded area around the emission profile. To look for any significant asymmetries, we overplotted the SW side of the disc on its NE side (red dotted line). This shows that there are no obvious signs of asymmetry within the allowed error bars. This plot also confirms that most of the emission is within 200 au. We also compare the gas disc emission to the continuum emission (green dashed line) and find that they are similar.

Finally, we have access to the gas kinematics by looking at the emission in the different channels that show the emission at a given radial velocity (±Δv, the channel width). In order to exploit the

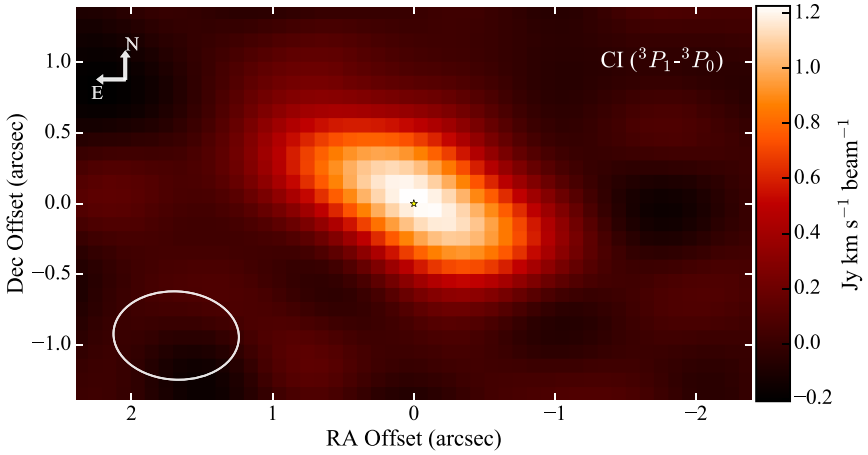

Figure 8. CI $^3P_0$–$^3P_1$ moment-0 (i.e. spectrally integrated) Briggs-weighted (robust = 0.5) CLEAN image of HD 131835 (in Jy km s^{-1} beam^{-1}). The *x*-axis shows the RA offset (in arcsec) from the star (shown by a yellow star symbol) and the *y*-axis the Dec offset (in arcsec). The ellipse shows the beam of 0.89 × 0.63 arcsec and the North and East directions are shown by the two arrows. The pixel size is 0.1 arcsec. We integrated the emission between −4 and 10 km s^{-1} to obtain the moment-0 image.

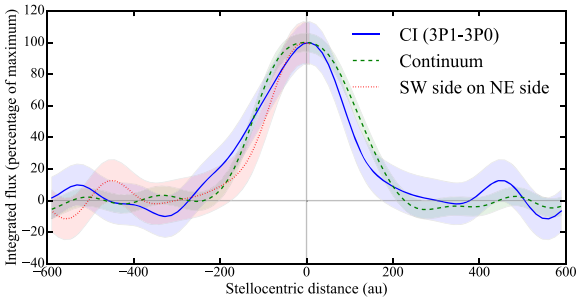

Figure 9. Radial profile of [CI] (blue solid line) and continuum (green dashed line) obtained by vertically averaging the moment-0 image shown in Fig. 8 and the continuum image from Fig. 5, respectively. We also look for asymmetries in the gas profile by overplotting the SW side of the gas disc on top of the NE side (red dotted line). The errors shown as transparent shaded area are 2σ. The profiles are normalized by their respective maximum.

extra information in velocity it is convenient to use a position-velocity (PV) diagram that is shown in Fig. 10. This is produced by rotating each slice of the [CI] data cube by the PA of the disc and averaging vertically over ±100 au. Each channel then corresponds to a horizontal line on the plot. The white lines shown in Fig. 10 correspond to the locations and radial velocities at which gas is expected to emit if on a circular orbit at 40 and 200 au (assuming a 1.77 $M_\odot$ star, Moór et al. 2015). The PV-diagram thus tells us that the bulk of the gas disc is between 40 and 200 au and a cavity or a depleted zone may be present interior to 40 au, which we will test further by comparing to models in the next Section 4.2.

Integrating the PV diagram along its *x*-axis, we obtain the emission spectrum shown in Fig. 11 at the channel width resolution ($\Delta v = 0.297$ km s^{-1}). The thin vertical line corresponds to a velocity of 3.57 km s^{-1} (which is the best-fitting value found from fitting the CI cube, see Section 4.2) and is close to the centre of the line.

4.2 Fit of the [CI] data

To model the gas data, we use the same approach as described in the previous Section 3.2 for the dust continuum. The only difference being that now we have to produce a cube for the image for the

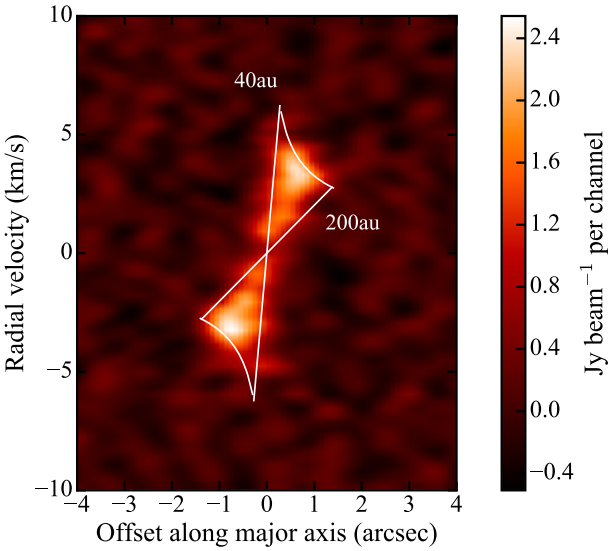

Figure 10. PV diagram of the [CI] gas disc around HD 131835. The white lines correspond to the locations and radial velocities at which gas is expected to emit if on a circular orbit at 40 and 200 au, respectively.

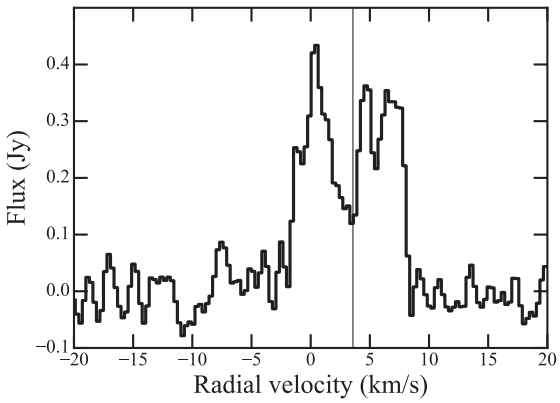

Figure 11. Spectrum of the [CI] line detected around HD 131835 at a resolution of 0.297 km s^{-1}. The thin vertical line corresponds to a velocity of 3.57 km s^{-1}.

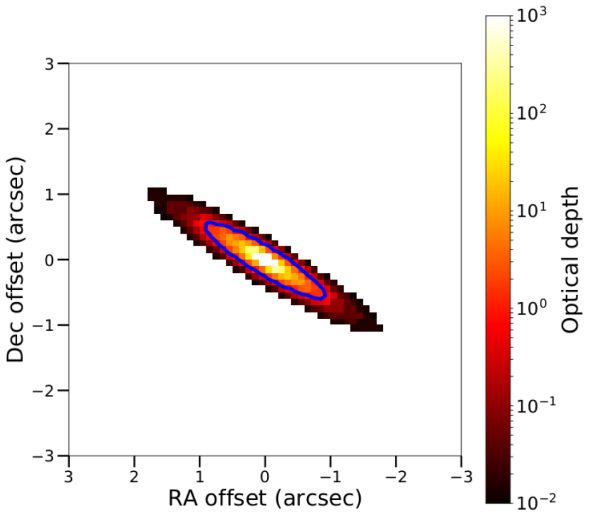

Figure 12. [CI] optical depth of the best-fitting model. The blue contour shows the $\tau = 1$ level.

different frequency channels (tracing different radial velocities of the gas). We also use RADMC-3D to produce the [CI] gas image and convert to visibilities using GALARIO (Tazzari et al. 2018) that can then be compared to the ALMA visibility data cube in an MCMC fashion.

We note that the [CI] emission predicted could be in the non-local thermal equilibrium (non-LTE) regime and thus we would have to add the collider density as an additional free parameter and take account of the radiation from the dust impinging on the gas. We first used the radiative transfer code LIME (Brinch & Hogerheijde 2010) that can handle non-LTE situations to check whether LTE is a good assumption for our case. We find that a good fit of the [CI] line only happens for C^0 masses that are high enough that LTE is a good assumption. Indeed, taking the worst-case scenario which is that electrons are only formed through carbon photoionization and not from other metals, with a low-ionization fraction, down to 10^{-2}, and are the only colliders, we find that LTE is still a good approximation. In Section 5.1, we give estimates of the ionization fraction in HD 131835 from a photodissociation region code and show that the ionization fraction depends on the exact content in carbon and it can vary from 10^{-5} to 10^{-1}. However, we find that including hydrogen collisions coming from H_2O photodissociation (if water is also released together with CO) would mean that LTE is reached even in the absence of electrons (as then hydrogen atoms can play the role of colliders). Indeed, the collision rates for hydrogen and C^0 are very similar to those of electrons with C^0. For a temperature between 10 and 200 K, the collision rates between H and C^0 are $\sim 1.7 \times 10^{-10}$ $cm^3\ s^{-1}$, which translates to a critical H density of ~ 300 cm^{-3} to be in LTE. This hydrogen density is small compared to what is expected in shielded discs, even for the case where only a small fraction of hydrogen is released together with CO (see Section 5.3). We thus assume that LTE is a good approximation even for very low carbon ionization fractions.

After investigation with LIME (and RADMC-3D), we also find that the [CI] line is optically thick for all the cases that match the observed data with an optical thickness >1 within 1 arcsec, where most of the emission is observed (see Fig. 12). This means that we will be able to find a good constraint on the gas temperature from the line fitting. As one LIME model takes about 10 min to compute, it would anyway be impossible to study a large parameter space in non-LTE and we instead use RADMC-3D in LTE that can compute image cubes in a few seconds and is thus suitable for an MCMC exploration.

We start by fitting for the inclination i, PA, and offsets to check that it is similar to the dust disc parameters (see Fig. A1). We also fit for the star radial velocity, which has been shown to be between 2 and 4 km s^{-1} (heliocentric frame) by previous studies (Moór et al. 2006, 2015). By comparing the posterior distributions of the gas and dust disc, we find that the inclination and PA of both discs are very similar. The astrometric offsets are also consistent between the two data sets. The best fit is for a stellar radial velocity around 3.57 ± 0.1 km s^{-1} (heliocentric frame), which is consistent with what has been found by previous studies (Moór et al. 2006, 2015) and shows that the gas is comoving with the star, as expected.

4.2.1 *Gaussian fit*

As the data does not show any hint of asymmetry, we assume an axisymmetric gas model. We first fit the data with a ring having a Gaussian radial profile as for the dust. Therefore, the surface density profile of the gas follows

$$\Sigma(R) = \Sigma_0 \exp\left(-\frac{(R-R_0)^2}{2\sigma_g^2}\right), \quad (4)$$

where Σ_0 is the surface density at R_0 and $\sigma_g = \Delta R/(2\sqrt{2\log 2})$, ΔR being the width (FWHM) of the gas disc. The scale height is fixed by the temperature such that $H = c_s/\Omega$, with the sound speed $c_s = \sqrt{kT/(\mu m_H)}$ and Ω the orbital frequency. The mean molecular mass μ could be much higher than in protoplanetary discs as the gas mass would be dominated by carbon and oxygen in H_2-depleted secondary gas discs. We have thus chosen $\mu = 14$ as in Kral et al. (2017c). The temperature profile is assumed to be a double power-law profile (motivated from Kral et al. 2016) defined by

$$T(R) = \begin{cases} T_0 \left(\frac{R}{R_0}\right)^{-\beta_1^t} & \text{for } R < R_0 \\ T_0 \left(\frac{R}{R_0}\right)^{-\beta_2^t} & \text{for } R > R_0. \end{cases} \quad (5)$$

The free parameters of this gas model are thus Σ_0, ΔR, T_0, β_1^t, β_2^t. The results are shown in Fig. 13 and the best-fitting parameters are listed in Table 2.

For this Gaussian radial profile, we find that the location of the gas disc $R_0 \sim 97^{+17}_{-8}$ au is consistent with that of the dust disc (~90 au). The FWHM of the gas disc is best fit by 86^{+18}_{-10} au, which is slightly larger than that derived for the dust disc ($\sim 75^{+10}_{-15}$ au) but is still consistent with being of the same radial extension within error bars.

The temperature at R_0 is best fit by $T_0 \sim 28$ K and a -1 radial power law. The best-fitting surface density of C^0 at R_0 is 1.7×10^{-5} kg m^{-2}, which corresponds to a column density of $\sim 10^{17}$ cm^{-2}, which is enough to start shielding CO (as seen in Section 2). This can also be translated into a number density $\Sigma_0/(2H\mu m_H) \sim 10^3$ cm^{-3}, assuming the best fit T_0 of ~28 K to derive H.

4.2.2 *Double power-law fit*

In the traditional unshielded secondary gas scenario picture, CO is expected to be colocated with the dust, because that CO is released from planetesimals that are traced by the dust seen in the ALMA continuum observations and photodissociates quickly, but this is not

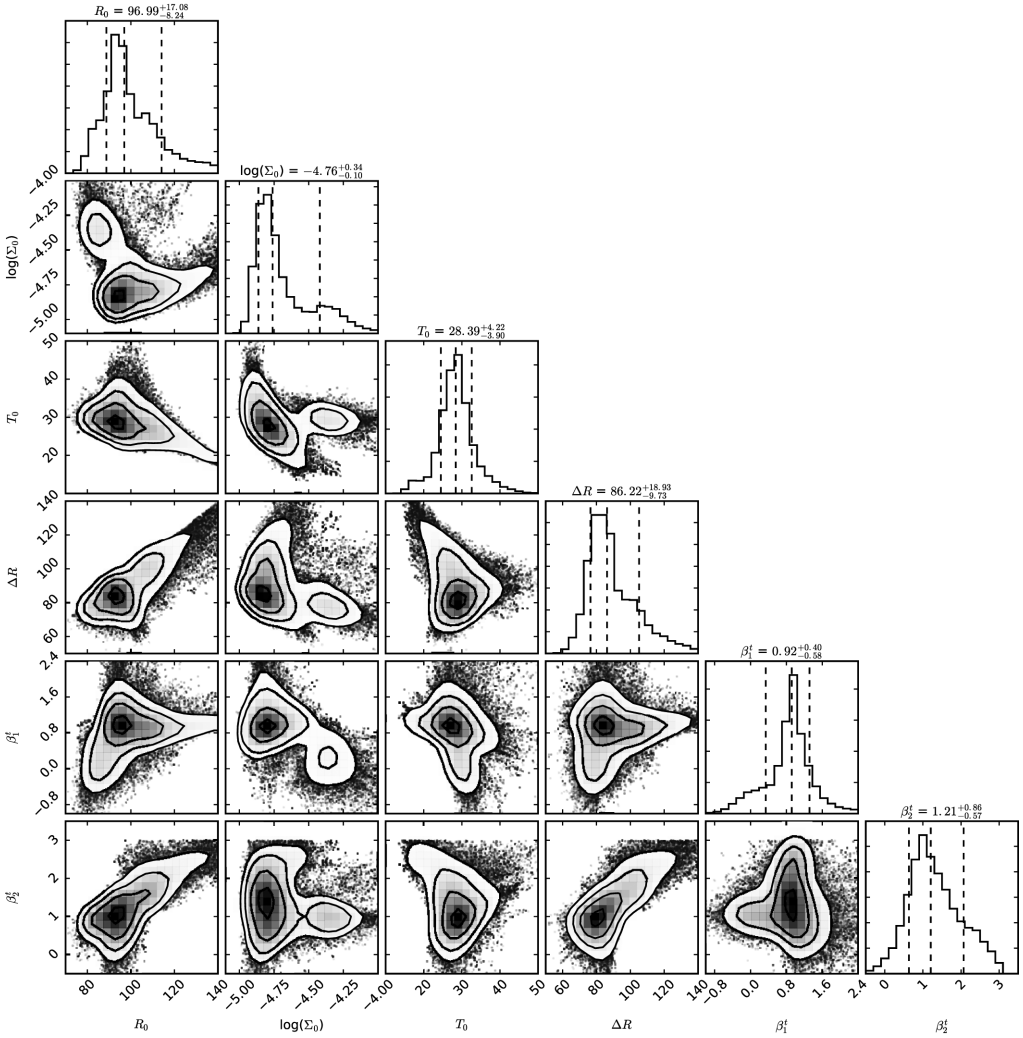

Figure 13. Posterior distribution of the Gaussian gas model for R_0, Σ_0, T_0, ΔR, β_1^t, β_2^t (see Section 4.2.1). The marginalized distributions are presented in the diagonal. The vertical dashed lines represent the 16th, 50th, and 84th percentiles.

Table 2. Table describing the best-fitting parameters of the Gaussian and double power-law [CI] gas modelling using an MCMC method (see Section 4.2). We list the median ± uncertainties, which are based on the 16th and 84th percentiles of the marginalized distributions.

Parameters	Best-fitting values	
	Gaussian	Double power law
R_0 (au)	97^{+17}_{-8}	118^{+19}_{-18}
$\Sigma_0/10^{-5}$ (kg m^{-2})	$1.7^{+2.1}_{-0.4}$	$1.2^{+2.2}_{-0.7}$
T_0 (K)	28^{+4}_{-4}	30^{+5}_{-4}
ΔR (au)	86^{+18}_{-10}	–
β_1^s	–	3.6^{+3}_{-3}
β_2^s	–	5.3^{+3}_{-4}
β_1^t	$0.9^{+0.4}_{-0.6}$	$-0.2^{+0.4}_{-0.3}$
β_2^t	$1.2^{+0.9}_{-0.6}$	$1.9^{+0.7}_{-1.6}$
i (deg)	–	$77^{+3.1}_{-2.4}$
PA (deg)	–	59^{+1}_{-1}
$v_\star$ (km s^{-1})	–	$3.57^{+0.1}_{-0.1}$

necessarily the case for shielded discs (as then CO can viscously spread, see Section 5.2.2). This is also not necessarily the case for carbon (neutral or ionized) that is not destroyed by photochemical processes and can evolve for longer, and may even spread viscously towards the central star as suggested by Xie et al. (2013) and Kral et al. (2016). To investigate the plausible larger extent of C^0, we now assume a double power-law radial profile for the gas density splitting at R_0. This model is motivated by the expected viscous evolution of C^0 (see Fig. 1). To be consistent, we also use the double power-law temperature profile splitting at R_0 described by equation (5). We define the surface density at R_0 to be Σ_0. The gas surface density is thus given by

$$\Sigma(R) = \begin{cases} \Sigma_0 \left(\frac{R}{R_0}\right)^{-\beta_1^s} & \text{for } R < R_0 \\ \Sigma_0 \left(\frac{R}{R_0}\right)^{-\beta_2^s} & \text{for } R > R_0 \end{cases} \quad (6)$$

and the temperature profile follows equation (5).

This leaves us with 10 free parameters that are R_0, Σ_0, T_0, β_1^s β_2^s, β_1^t, β_2^t, i, PA, and $v_\star$. We explore the parameter space with the same MCMC procedure as presented for the continuum and previous gas Gaussian profile and the results are shown in Fig. 14. The best-fitting parameters are also summarized in Table 2.

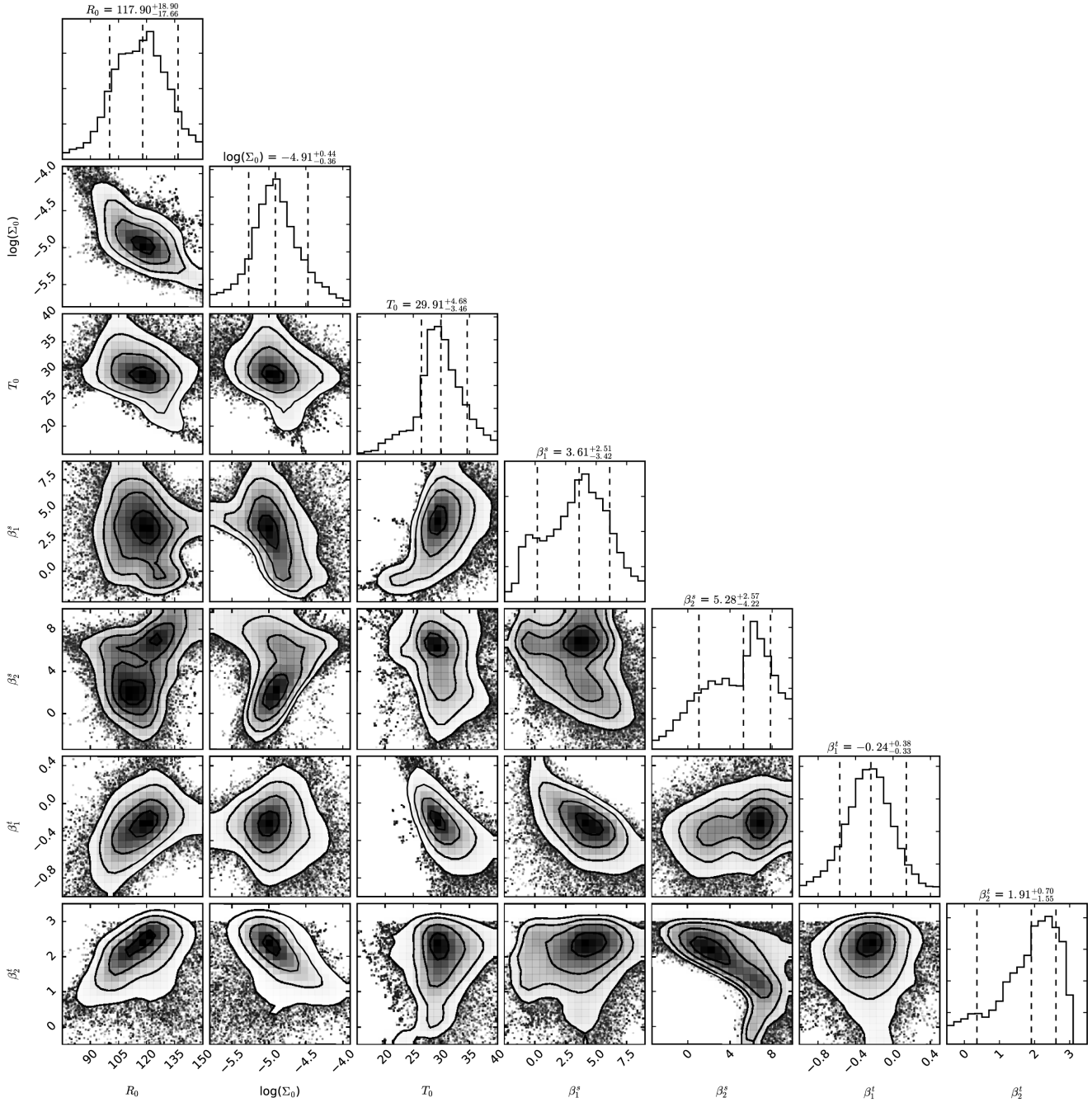

Figure 14. Posterior distribution of the double power-law gas model for R_0, Σ_0, T_0, β_1^s, β_2^s, β_1^t, β_2^t (see Section 4.2.2). The marginalized distributions are presented in the diagonal. The vertical dashed lines represent the 16th, 50th, and 84th percentiles.

We find that the gas disc is likely to be peaking in surface density at $R_0 \sim 118$ au but the error bars are large ($\pm$19 au) because of the low spatial resolution and due to a slight degeneracy with Σ_0, the surface density at R_0. Indeed, if an optically thick gas disc is moved at a greater distance from the star but with a smaller surface density, the integrated flux over the beam can still be the same as the original disc. The best-fitting surface density at R_0 is $1.2^{+2.2}_{-0.7} \times 10^{-5}$ kg m^{-2}, which corresponds to a column density of $\sim 6^{+11}_{-3} \times 10^{16}$ cm^{-2}, which is enough to start shielding CO (as seen in Section 2). This can also be translated into a number density $\Sigma_0/(2H\mu m_H) \sim 0.6^{+1.1}_{-0.3} \times 10^3$ cm^{-3}, assuming the best-fitting T_0 of $\sim$30 K and $R_0 \sim 110$ au to derive H.

The slope of the surface density for $R > R_0$, i.e. β_2^s, is not well constrained but is best fit by a steep value close to 5. This means that there may not be much mass hiding beyond R_0. Despite the uncertainties, the probable steepness of the slope is however helpful to constrain the models as it suggests that the gas disc has not reached steady state. Indeed, the outer surface density slope might be too steep compared to a steady state decretion profile. At steady state, we expect (see equation 1) the accretion profile ($R < R_0$) surface density to scale as R^{-n} and the decretion profile ($R > R_0$) as $R^{-n-1/2}$, where n is the radial scaling in viscosity, i.e. $\nu \propto R^n$ (Metzger et al. 2012). For a temperature profile in $R^{-\beta}$, as $n = 1.5 - \beta$, it means that for $\beta = 1/2$, $\Sigma \propto R^{-1}$ for $R < R_0$, and $\Sigma \propto R^{-3/2}$ for $R > R_0$. If

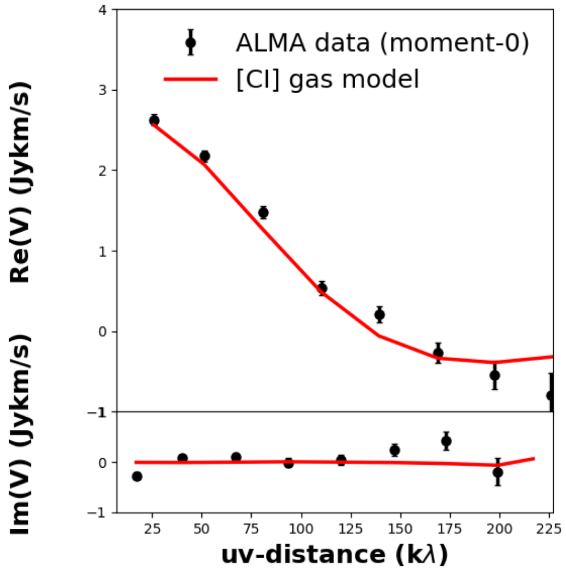

Figure 15. Real part (top) and imaginary part (bottom) of the [CI] gas moment-0 (integrated across the different channels) visibilities (black dots with errors bars) along with the best-fitting model (overplotted red line) described in Section 4.2 and whose parameters are given in Table 2. The uv-distances are given in units of observing wavelength and moment-0 visibilities in Jansky km s^{-1}.

we assume that $\beta_2^t = 3/2$, the steady state surface density decretion profile should scale as $R^{-1/2}$, therefore if a profile as steep as $\Sigma(R > R_0) \propto R^{-5}$ is confirmed, this would imply that steady state is not reached, which is most likely the case here (see also Section 2). But we note that within the error bars, we cannot entirely rule out a steady state profile. Only higher resolution observations would settle this matter.

For $R < R_0$, β_1^s is also not well constrained, except to be > -2.5 (at the 99.7 per cent level). This is because the line is becoming optically thick quite rapidly and thus adding more mass in the inner region does not increase the emergent intensity. It is therefore hard to tell from the inner accretion profile whether the gas disc is at steady state for which higher spatial resolution observations would again be necessary.

We have also run another MCMC simulation where we added another free parameter $R_{\rm min}$ (on top of the double power-law model) below which the surface density becomes zero. We find that an upper limit of $R_{\rm min} = 35$ au can be set, meaning that gas is needed to extend at least to 35 au to explain the data. However, values of $R_{\rm min} < 35$ au are not ruled out by the fitting process and it may well be that the gas disc extends further inwards (an observation at higher resolution would also be needed to constrain that better). The gas disc is thus at a minimum spanning the range 35–100 au, which is slightly more extended (taking into account error bars for the dust model) than the dust disc in the inner regions and could as well be in the outer regions. This favours that the gas had time to viscously spread since it has been produced.

The temperature T seems to be well constrained to around 30 K ($\pm$4 K) in the whole disc (at least for $R < R_0$ where β_1^t is close to zero). A good constraint arises because the line is optically thick (see Fig. 12) and the observed emission depends only on the temperature and the surface area of emission, which is fixed by the geometry of the disc. In the outer regions, the temperature drops with $\beta_2^t > 0$.

We compare the best-fitting model to the observations in the visibility space by plotting the moment-0 visibilities in Fig. 15 (i.e. the visibilities in each channel are summed together), even though the best fit was found by fitting each of these different channels.The model represents well the overall shape of the visibilities, but leaves a few significant residuals probably linked to the detailed structure of the emission.

This physical modelling of the [CI] data allows us to place some constraints on the neutral carbon mass around HD 131835. Indeed, we find that the best fit is for a mass $M_{\rm C^0} = 3.1 \times 10^{-3}$ M$_\oplus$. From the MCMC, we find that $2.7 \times 10^{-3} < M_{\rm C^0} < 1.2 \times 10^{-2}$ M$_\oplus$ (16th and 84th percentiles), assuming that $\beta_1^s < 3$. Higher values of β_1^s would be unphysical because the steady state level for the range of temperature slopes $\beta = [-1, 0]$ derived from the MCMC are expected to be in $R^{\beta - 3/2}$ (see equation (1)). The C^0 mass is not well constrained because the line is optically thick in the whole disc but we will show in Section 5.2.3 that in order to match the CO mass derived from an ALMA optically thin line observation (Moór et al. 2017) with this C^0 mass imposes a narrower range of C^0 masses. We note that the C^0 mass derived here is in the right range of values to be able to start shielding CO from photodissociating as can be seen from Fig. 3 presented in the introduction of shielded discs (see Section 2.2).

5 DISCUSSION

5.1 Temperature, ionization fraction, and chemical reactions expected for a shielded disc of secondary origin

From our modelling of the [CI] line, we find that $2.7 \times 10^{-3} < M_{\rm C^0} < 1.2 \times 10^{-2}$ M$_\oplus$. The C$^+$ upper limit from Herschel (at 30 K, assuming LTE) is 2×10^{-3} M$_\oplus$ (Moór et al. 2015). This means that the upper limit on the ionization fraction is $\sim$0.4, which is already lower than that found for β Pic (Cataldi et al. 2014, 2018). We now use the DALI 2D code[4] (Bruderer et al. 2012; Bruderer 2013) to compute the carbon ionization fraction in the disc taking into account the UV flux from the central star and IRF. For the DALI simulations, we start with a cometary abundance of hydrogen, carbon, and oxygen (i.e. for a carbon abundance set to 1, then $N_{\rm H} = 20$ and $N_{\rm O} = 11$). We set a star spectrum similar to HD 131835, i.e. a 15 Myr A-type star of about 10 L$_\odot$. We impose that the total carbon mass is around 10^{-2} M$_\oplus$ and has a constant surface density between 1 and 100 au (with an aspect ratio of 0.1), which is consistent (within error bars) with values derived from the [CI] observations. Each simulation takes a day to compute and we clearly cannot iterate to a best-fitting model but we use the simulations to have a feel for the typical ionization fraction and temperature to expect in these shielded discs.

Fig. 16 (left) shows the result of the simulation for the ionization fraction. We expect that in the mid-plane of the disc and beyond 10 au, the ionization fraction can become very small ($\sim 10^{-5}$) owing to C^0 shielding that catches most of the UV photons from the IRF in the upper layer so that the mid-plane cannot be ionized. Within 10 au, the ionization fraction goes back up because of the UV photons coming from the star. We note that our grid started at 1 au and we

[4]The low gas density and very low abundance of hydrogen in the system we study is strictly outside the parameter range for which DALI – a protoplanetary disc code – is validated to give correct results. We caution the reader to interpret our results as a guide to future work rather than a final result for the HD 131835 disc.

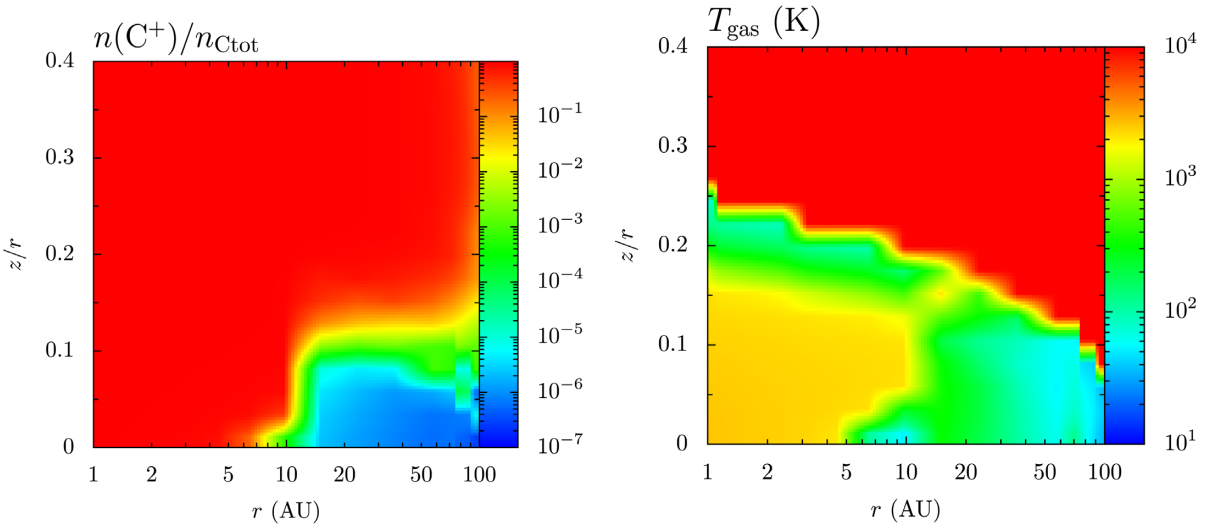

Figure 16. *Left:* Ionization fraction of carbon in a shielded disc simulated with the DALI code. z is the vertical direction in the disc. *Right:* Gas temperature in a shielded disc simulated with the DALI code.

expect that this is an effect of the grid because the radial optical depth would be much higher for a grid starting at the star location and therefore UV photons from the star would be caught at a much smaller radius, thus decreasing the ionization fraction below 10 au. Our assumption that the ionization fraction is low in these discs, lower than 0.1, seems to be justified from this test simulation. We also note that we ran some simulations with 10 times less carbon and the ionization fraction was becoming higher, closer to 0.1. It is therefore dependent on the exact carbon mass at different radii. Higher resolution images would enable us to pinpoint the carbon density as a function of radius and compute a better estimate of the ionization fraction in the disc.

Fig. 16 (right) shows the simulation results for the temperature in a typical shielded disc (i.e. with enough carbon to shield CO over long time-scales). We find that, indeed, the temperature can reach values of order 30–40 K in the mid-plane close to 100 au. This is in agreement with the temperature obtained from fitting the optically thick [CI] line in Section 4.2. We note that the temperature can indeed be lower than the dust temperature (which would be around 50 K at 100 au around a star similar to HD 131835 assuming black body emission). By looking at what is setting the temperature, we find that the dominant heating is from C^0 photoionization and the dominant cooling is from the OI and CII lines.

CO is not the only molecule that can be shielded owing to C^0. In the DALI simulations, we find that CN, N_2 as well as CH^+ are also shielded by C^0 and thus, they can accumulate over time. This effect can be quantified using the results from the study by Rollins & Rawlings (2012). Similar to the photodissociation time-scale of CO used in equation (2), Rollins & Rawlings (2012) find that C^0 shielding increases the photodissociation time-scales of CN, N_2, and CH^+ as $1/(S + (1 - S)\exp(-\sigma_i N_{C^0}))$. While $S = 0$ in equation (2) for CO, it is equal to 0.018, 0, and 0.036 for CN, N_2, and CH^+, respectively. This means that for these three molecular species, C^0 shielding can be almost as strong as for CO. We thus predict that the photodissociation time-scales of these species, respectively, 60, 190, and 100 yr (assuming photons coming from the IRF, van Dishoeck 1988) could be orders of magnitude longer than expected in unshielded discs (see Matrà et al. 2018a), which may lead to these species being detectable in shielded discs together with C^0. CH^+ would be particularly interesting to detect as it would give some constraints on the amount of hydrogen in the system (as it would mainly come from C + H) and potentially on the amount of water on the planetesimals.

5.2 New models to refine the total C^0 mass and viscosity (α) in the gas disc

In this section, we first start by presenting a new analytical model of shielded discs that takes into account the shielding of CO by C^0 and shows what range of α or $\dot{M}_{CO}$ values can lead to a shielded configuration (Section 5.2.1). This analytical model can be useful to understand the different scalings but it lacks accuracy as it neglects CO self-shielding. That is why we then develop a more sophisticated semi-analytical box model in Section 5.2.2 that takes into account CO self-shielding and shows the temporal evolution of the build-up of gas at the radius R_0 of gas injection. We use this more accurate model in Section 5.2.3 to fit the observed CO mass in HD 131835 and find what typical α value is needed to explain the data. In turn, it provides the C^0 mass that can accumulate for a given α and CO production rate that we can compare to our new CI observations finding that indeed our model is consistent with both CO and CI data. We note that this refined model is 0D but could be improved by turning it into a 1D model in the future as it would be useful when higher resolution observations are at hand. For the data we have, such a model would not be useful and is therefore deemed beyond the scope of this paper.

5.2.1 An analytic model

As previously explained in Section 4.2, the C^0 mass is not well constrained from the [CI] observation we presented but assuming that the gas produced is secondary, we can improve the constraints on the C^0 mass using our knowledge of the much more accurate CO mass (since this was measured from an optically thin line) and computing the C^0 mass that would be required to explain this amount of CO. With the knowledge of this more accurate (model-based) C^0 mass, we can then put some constraints on the

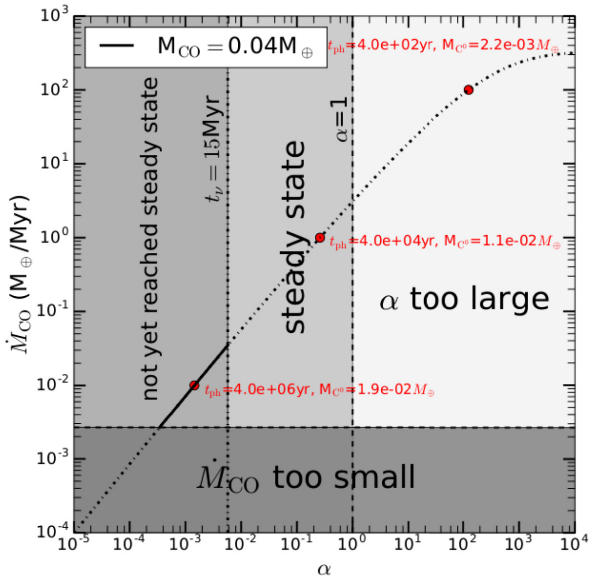

Figure 17. The dash-dotted black line shows the α value needed to produce enough C^0 that can shield CO and produce a total CO mass of 0.04 $M_\oplus$ as a function of the production rate of CO in the belt $\dot{M}_{CO}$. The two vertical lines show $\alpha = 1$ (dashed), and $\alpha = 6 \times 10^{-3}$ (dotted) corresponding to a viscous time-scale of 15 Myr (i.e. the age of HD 131835). The horizontal dashed line shows the minimum value of $\dot{M}_{CO}$ to have been able to produce 0.04 $M_\oplus$ of CO within 15 Myr. The three red points show the corresponding photodissociation time-scales and C^0 masses for three different α values corresponding to $\dot{M}_{CO} = [10^{-2}, 1, 10^2] M_\oplus$ Myr^{-1}, respectively. The solid section of the dash-dotted line shows the α range that can explain the CO and C^0 observations within the frame of our analytical model described in Section 5.2.1.

viscosity (parametrized with α) that would allow such a C^0 mass to accumulate over the age of the system.

Assuming that CO is produced at a rate $\dot{M}_{CO}$ and that the CO mass required to fit the observations is M_{CO}, a photodissociation time-scale $t_{CO} = M_{CO}/\dot{M}_{CO}$ is required. Using equation (2), this translates to the C^0 mass needed to shield CO

$$M_{C^0_n} = \frac{2\pi R \Delta R \mu_c m_H}{\sigma_i} \ln\left(\frac{M_{CO}}{120\text{yr} \times \dot{M}_{CO}}\right), \quad (7)$$

where $\dot{M}_{CO}$ should be expressed in units of mass per yr and μ_c is the mean molecular weight of carbon. The C^0 mass is set through the CO input rate such that $\dot{M}_{C^0} = 12/28(1-f)\dot{M}_{CO}$, where f is the ionization fraction. C^0 at R_0 is assumed to evolve to steady state over local viscous time-scales such that to get the C^0 mass needed $M_{C^0_n}$, the local viscous time-scale should be $t_\nu(R_0) = M_{C^0_n}/\dot{M}_{C^0} = R_0^2/(12\nu(R_0))$, where $\nu = \alpha c_s^2/\Omega$ is the viscosity parametrized by an α parameter. This translates as a condition on α to get the C^0 mass needed and therefore the CO mass required

$$\alpha = \frac{\mu \sigma_i \sqrt{G M_\star} \dot{M}_{CO}(1-f)}{56\pi \mu_c \Delta R k T_0 \sqrt{R} \ln\left(\frac{M_{CO}}{120\text{yr} \times \dot{M}_{CO}}\right)}. \quad (8)$$

Fig. 17 shows the value of α that is required to produce a C^0 mass that can produce the observed 0.04 $M_\oplus$ of CO for different values of $\dot{M}_{CO}$ for a disc located at $R_0 = 90$ au with, again, a width $\Delta R = 70$ au. To the right of the black dash dotted line, the CO mass produced would be below 0.04 $M_\oplus$ (because α is so high that there is insufficient C^0 to shield CO); similarly more CO would be expected to the left of the line. There are four different regimes shown on the plot with different grey shaded areas. At the extreme right of the plot, $\alpha > 1$ and is therefore too large to be physical. In the middle, this is the regime where the gas disc has had time to reach steady state. At the extreme left of the plot, α is small and the gas disc has not yet had time to reach steady state. The viscous time-scale must be >15 Myr (age of the system) to not be at steady state, which corresponds to $\alpha < 6 \times 10^{-3}$. The horizontal dashed line shows the minimum value of $\dot{M}_{CO}$ to have been able to produce a total CO mass of 0.04 $M_\oplus$ over 15 Myr.[5] We also showed in Section 4.2 that the gas disc is most likely not at steady state as the outer surface density slope may be too steep and thus the disc could have spread only for a maximum of 15 Myr (likely much less as secondary production of gas presumably starts when the protoplanetary disc is dispersed, i.e. after a few Myr).

To respect all the constraints so far, we are thus left with the part of parameter space shown by the solid line, i.e. $2.5 \times 10^{-4} < \alpha < 6 \times 10^{-3}$ and $2 \times 10^{-3} < \dot{M}_{CO} < 4 \times 10^{-2}$ $M_\oplus$ Myr^{-1}. For instance, we calculate the corresponding CO photodissociation time-scale and C^0 mass for $\dot{M}_{CO} = 10^{-2}$ $M_\oplus$ Myr^{-1} (the leftmost red point) that are 4 Myr and 1.9×10^{-2} $M_\oplus$, respectively (which is for $\alpha = 1.5 \times 10^{-3}$). The C^0 mass obtained is thus compatible with the C^0 mass derived from observations in Section 4.2. We note that in the process of converting $\dot{M}_{CO}$ to a C^0 input rate (to then work out the α value needed to explain the observed CO mass), we assumed an ionization fraction f of 0.1. However, this does not affect the results because the dependence is in $1 - f$ and f is assumed to be <0.1 as already discussed in Section 5.1.

The range of $\dot{M}_{CO}$ expected for HD 131835 from a secondary gas production model can be derived from the dust luminosity using equation (2) in Kral et al. (2017c) and does not depend on the photodissociation time-scale. This calculation finds $10^{-2} < \dot{M}_{CO} < 0.5$ $M_\oplus$ Myr^{-1} by assuming a CO-to-dust mass ratio on the comets between 1 and 30 per cent (i.e. similar to the range observed for Solar System comets, Mumma & Charnley 2011) but we caution that the uncertainties can be up to a factor 10 on this range (Kral et al. 2017c). This predicted range and the plausible $\dot{M}_{CO}$ range needed overlap and are thus compatible, which gives confidence that a secondary model can indeed explain the dust, neutral (and ionized) carbon and CO observations all together.

The derived value of α is much smaller than that derived in the β Pic gas disc (for which we found $\alpha > 0.1$, Kral et al. 2016). However, this might be expected for the gas disc around HD 131835 owing to the optical thickness to UV photons that can ionize carbon resulting in a much lower ionization fraction and thus a lower α value if the viscosity is triggered by the magnetorotational instability (Balbus & Hawley 1998; Kral & Latter 2016, and references therein). This low-α value could also come from non-ideal MRI effects as a lower ionization fraction may result in ambipolar diffusion becoming important, thus slowing down the viscous evolution (see Kral & Latter 2016). In any case, this lower value of α is compatible with the wide range of values found in protoplanetary discs (e.g. between 10^{-4} and 0.04 as estimated in Rafikov 2017).

[5]We note that there is also a maximum production rate if we assume that the whole belt mass, which cannot be more massive than the solid mass available in protoplanetary discs (i.e. $\sim 0.1 \times M_\odot/100 \sim 300$ $M_\oplus$ assuming a gas-to-dust ratio of 100), is released in CO over 15 Myr, which would give ~ 20 $M_\oplus$/Myr.

5.2.2 A more refined semi-analytic model

The analytic model described in Section 5.2.1 is now improved to take into account the temporal evolution of the gas as well as CO self-shielding that can become important for the high CO masses involved. Now, we also include a negative feedback on the total C^0 mass, which is that for an increasing C^0 mass, CO has time to viscously spread (because of the longer photodissociation time-scale) and thus less C^0 is produced from CO at a given radius (which means CO destruction and C^0 production cannot be assumed to be constant in time). The previous section should therefore just be used to get an idea of the different scalings but not to compute predictions. For the new refined semi-analytic model, we start with no gas at $t = 0$ and input a constant CO gas mass $\dot{M}_{\rm CO}$ per unit time. The CO mass $M_{\rm CO}$ is then evolved over time at the radius R_0 as

$$\frac{{\rm d}M_{\rm CO}}{{\rm d}t} = \dot{M}^{+}_{\rm CO} - \dot{M}^{-}_{\rm CO}, \tag{9}$$

where $\dot{M}^{+}_{\rm CO} = \dot{M}_{\rm CO}$ is the production rate of CO and $\dot{M}^{-}_{\rm CO} = M_{\rm CO}/t_{\rm COremoval}$ is the destruction rate of CO, with $t_{\rm COremoval} = (1/(t_{\rm COph}) + 1/t_{\nu})^{-1}$, where $t_{\rm COph}$ includes the photodissociation time-scale due to C^0 shielding (equation 2) and self-shielding (tabulated from Visser et al. 2009).

In a similar way, the carbon mass $M_{\rm C}$ follows

$$\frac{{\rm d}M_{\rm C}}{{\rm d}t} = \dot{M}^{+}_{\rm C} - \dot{M}^{-}_{\rm C}, \tag{10}$$

where $\dot{M}^{+}_{\rm C} = (12/28)M_{\rm CO}/t_{\rm COph}$ and $\dot{M}^{-}_{\rm C} = M_{\rm C}/t_{\nu}$.

We evolve this set of equations for 30 Myr for different α values (10^{-1} and 10^{-3}) and different $\dot{M}_{\rm CO}$ (10^{-1} and 10^{-3} $M_\oplus$ Myr^{-1}) and the resulting CO and C^0 masses are plotted in Fig. 18 in blue and orange, respectively. Motivated by our previous results, for these plots we assume that $R_0 = 90$ au, the ionization fraction is close to 0, the temperature is ∼30 K, and the planetesimal belt spreads over $\Delta R = 70$ au. The classical unshielded case, where shielding of CO by C^0 is unimportant is shown in the bottom left panel of Fig. 18. This happens for high α values or low $\dot{M}_{\rm CO}$. In this case, we see that the steady state CO mass (which is 120 yr $\times$ $\dot{M}_{\rm CO} = 1.2 \times 10^{-7}$ $M_\oplus$ and shown as a blue horizontal dotted line) is reached in less than 500 yr. The C^0 mass accumulates until reaching a few viscous time-scales (which is ∼0.1 Myr for $\alpha = 0.1$) when the viscous spreading balances the carbon input rate. The final C^0 mass reached is $\dot{M}_{\rm C^0} t_{\nu} = 3.6 \times 10^{-5}$ $M_\oplus$ as shown by the horizontal orange dotted line.

The other case for which $\dot{M}_{\rm CO} = 10^{-3}$ $M_\oplus$ Myr^{-1} (bottom right plot) is very similar but eventually the C^0 mass becomes large enough that C^0 starts shielding CO from photodissociating (the C^0 shielding mass above which this happens is shown as a horizontal orange dashed line, which is taken to be when $\sigma_i N_{\rm C^0} = 1$ in equation (2) and is close to 2×10^{-3} $M_\oplus$ as shown in Fig. 3). This is why after ∼1 Myr, the CO mass goes back up again before plateauing to its new steady-state value. This starts happening because the maximum C^0 mass that can be reached is higher than the mass to start shielding CO (i.e. $\dot{M}_{\rm C^0} t_{\nu} > 2\pi R \Delta R \mu_c m_H / \sigma_i$), which was not the case previously for a higher α.

The top left plot is for a higher CO input rate (and high α) and it evolves similarly to the case that has just been presented, except for the intermediate plateau that is now affected by CO self-shielding. The blue horizontal dashed line at 8×10^{-5} $M_\oplus$ is when the CO photodissociation time-scale is increased due to self-shielding by e ∼ 2.72 but self-shielding starts affecting the CO mass before CO reaches that level, and this further increases the CO lifetime.

The top right subplot in Fig. 18 is the most characteristic of what could explain shielded discs (note the more extended y-scale for this subplot). In this case, the C^0 mass that can be reached is two orders of magnitude above where C^0 starts shielding CO, meaning that the exponential term in equation (2) can reach very high values and therefore CO can survive several orders of magnitude longer than without shielding. The CO mass that is reached for this case is ∼0.8 $M_\oplus$, i.e. more than 4 orders of magnitude higher than the expected mass of $\sim 10^{-5}$ $M_\oplus$ without shielding. For this case, shielding from C^0 dominates over self-shielding. The shielding time-scale becomes so long that the maximum CO mass that can be reached becomes dominated by viscous spreading, which is why the CO mass plateaus at $\dot{M}_{\rm CO} t_{\nu} \sim 0.8$ $M_\oplus$ (blue dash-dotted line). The C^0 mass does not reach its maximum theoretical value of $\dot{M}_{\rm C^0} t_{\nu}$ (orange dotted line) because CO spreads more rapidly than it is photodissociated and thus the maximum C^0 mass that can be reached is a factor $\sim t_{\nu}/t_{\rm COph}$ smaller. This also means that as CO spreads viscously, it is not necessarily colocated with the main dust belt (as was originally thought for gas discs of secondary origin), but it should in any case be colocated with the carbon gas disc (at least in the region where C^0 shielding is efficient, i.e. this colocation may not apply at large radii, see Fig. 1).

Fig. 19 shows the CO (top) and C^0 (bottom) gas masses after 1, 3, 10 Myr (thin lines) and 30 Myr (thick) as a function of α for three different $\dot{M}_{\rm CO}$ of 10^{-1} (solid), 10^{-2} (dashed), and 10^{-3} $M_\oplus$ Myr^{-1} (dotted). For high α values (or low $\dot{M}_{\rm CO}$), the final CO mass reached is 120 yr $\times$ $\dot{M}_{\rm CO}$, as expected without shielding and the C^0 mass reaches its maximum at a value of 12/28 $\dot{M}_{\rm CO} t_{\nu} \propto \dot{M}_{\rm CO}/\alpha$, which explains the C^0 evolution with α and $\dot{M}_{\rm CO}$. When α becomes smaller or $\dot{M}_{\rm CO}$ becomes higher, a new regime is attained where the CO mass reaches orders of magnitude higher values which can explain the typical CO masses observed with ALMA for shielded discs. The final CO mass in this regime plateaus because it is then dominated by the viscous evolution since the photodissociation time-scale becomes greater than the viscous time-scale. In this shielded regime, the C^0 mass plateaus because the CO mass input rate at R_0 becomes lower owing to CO spreading and thus less C^0 can be produced per unit of time.

Therefore, this figure shows that there is clearly two regimes of secondary gas production with a sharp transition between gas discs of low CO and C^0 masses (e.g. β Pic) and high CO and C^0 masses (e.g. HD 131835) depending on α and $\dot{M}_{\rm CO}$. However, we notice that if the gas production only started recently (i.e. ∼1 Myr, lowermost thin lines on Fig. 19) and for low values of $\dot{M}_{\rm CO}$, a disc that is on its way to becoming shielded could be mistaken for an unshielded low-mass secondary gas disc. This is because before becoming a high mass gas disc, there is a build-up process, the time-scale of which is fixed by the time to reach a C^0 mass high enough to start shielding CO as shown in Fig. 18. Also, we note that the gas input rate will decrease over time because the dust mass-loss rate will become smaller owing to collisions that are depleting the belt mass (e.g. Wyatt et al. 2007; Löhne, Krivov & Rodmann 2008). Thus, a shielded disc can become unshielded again after a certain period of time.

5.2.3 Application of the refined semi-analytic model to HD 131835

We now apply the model presented in the previous Section 5.2.2 to the specific case of HD 131835 and try to explain the high observed CO mass of 0.04 $M_\oplus$ in this system. We ran a grid of 1000 models

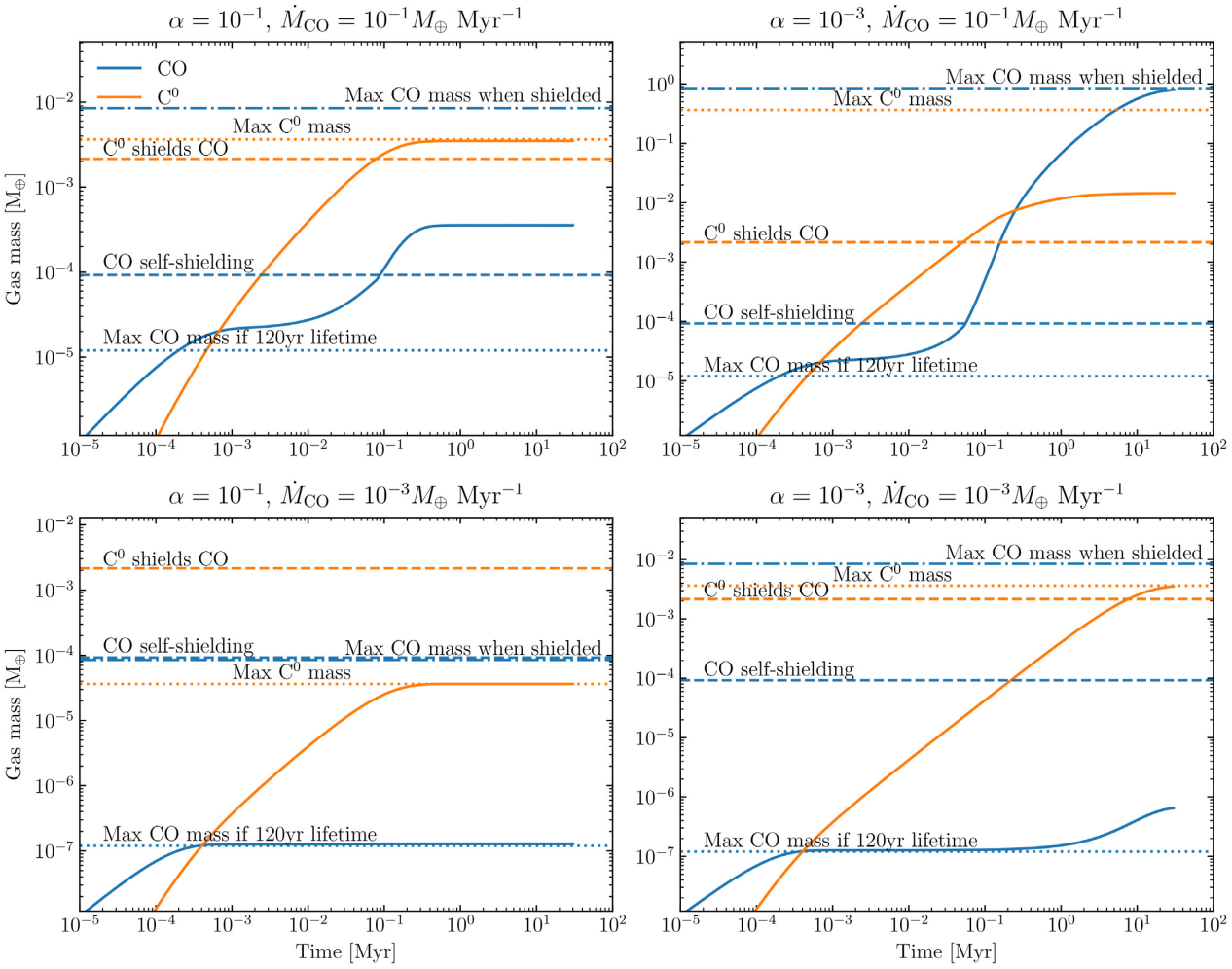

Figure 18. CO (blue) and C^0 (orange) gas mass evolution as a function of time for different $\dot{M}_{\rm CO}$ (10^{-3}, and 10^{-1} M$_\oplus$ Myr^{-1}) and α values (10^{-3} and 10^{-1}). The dotted horizontal blue line shows the maximum CO mass that can be reached if the CO lifetime is 120 yr (i.e. no shielding) and the orange one is the maximum C^0 mass that can be reached when viscous spreading balances the C^0 input rate. The dashed horizontal blue (orange) line shows when CO self-shielding (C^0 shielding of CO) becomes important. The dash-dotted blue line is the maximum CO mass that can be reached when CO is shielded and that the viscous time-scale becomes smaller than the photodissociation time-scale, i.e. this CO mass is when viscous spreading balances the CO input rate. For these plots, we assumed that $R_0 = 90$ au, $T = 30$ K, and $\Delta R = 70$ au.

for different $\dot{M}_{\rm CO}$ and α values and in Fig. 20 (top), we compute the predicted CO mass shown in colour-scale and plot contours that show where the predicted CO mass is within 1, 3, and $5\sigma_{\rm CO}$ from the mass inferred from the observations, where the uncertainty $\sigma_{\rm CO}$ is assumed to be 0.5 dex from the observed mass (Moór et al. 2017). As the models are not always at steady state, we ran simulations for different ages. HD 131835 is ∼15 Myr old but the secondary production started after the protoplanetary disc dispersed, i.e. likely after a few Myr. We plot the best-fitting models for 3, 10, and 30 Myr. 10 Myr is likely to be the most realistic unless the gas production is linked to a recent event (a few Myr old) and we also show 30 Myr when most of the parameter space is then at steady state. The horizontal part of the best-fitting region (i.e. where the contours are horizontal for small α) is for models that have not reached steady state yet. The yellow region shows where the C^0 mass produced through the secondary evolution is not high enough to shield CO from photodissociating (i.e. it is not the shielded disc regime). In the rest of the parameter space, CO is shielded owing to C^0 and the contours show where the CO mass is closest to 0.04 M$_\oplus$. The green dashed line shows the CO production rate predicted from the stellar and dust disc parameters (see Matrà et al. 2017b, noting that uncertainties are up to a factor 10 on that value). From the 10 Myr plot, we conclude that $10^{-3} < \alpha < 10^{-2}$ can explain the observed CO mass, which is similar to what was found with the more simple analytical model presented in Section 5.2.1 as can be seen from the blue dashed line (on top plots of Fig. 20) representing the analytical model developed in Section 5.2.1.

We then compute the C^0 mass that is needed to explain that CO mass on the bottom row of Fig. 20 (the red and purple lines are for 2.7×10^{-3} and 1.2×10^{-2} M$_\oplus$, respectively, corresponding to the range of plausible masses derived from observations). We find that by overplotting the best-fitting contours for CO mass from the top plot on the bottom one, then for 10 Myr, the C^0 mass needed to explain the observed CO mass is between 5×10^{-3} and 10^{-2} M$_\oplus$, which is similar to what we deduced from the [CI] observations in Section 4.2 but is slightly narrower. We find that the best fit is not necessarily at steady state. If $\alpha \sim 10^{-3}$, the disc surface density is still evolving with time as can be inferred from the fact that the

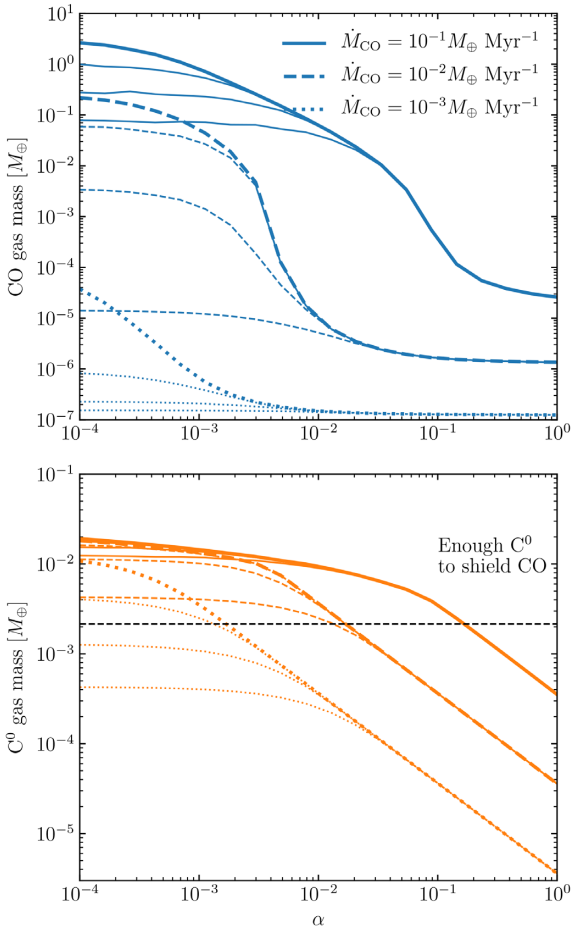

Figure 19. CO (top) and C^0 (bottom) gas masses after 1, 3, and 10 Myr (thin lines) and 30 Myr (thick) as a function of α for three different $\dot{M}_{\rm CO}$ of 10^{-1} (solid), 10^{-2} (dashed), and 10^{-3} $M_\oplus$ Myr^{-1} (dotted). This shows the final stages of gas evolution depicted in Fig. 18 for a wider variety of α and $\dot{M}_{\rm CO}$. We keep the blue and orange colours for CO and C^0, respectively, to match the convention used in Fig. 18. The horizontal dashed line in the bottom plot shows when the C^0 mass becomes high enough to start shielding CO significantly.

contours are horizontal in this range. We note that even for larger α, the inner and outer regions are not necessarily at steady state (even though it is not on the horizontal part anymore) because the global viscous time-scale can be ∼10 times longer than the local viscous time-scale for which steady state is reached at R_0 only (Pringle 1981), i.e. the gas disc can be at steady state in the parent belt but not yet in the inner/outer regions. As noted in Section 4.2, as the outer radial profile of the gas density is very steep, it could be that the gas disc has not reached steady state and thus the global viscous time-scale should be <15 Myr (the age of the system), which translates as $\alpha < 6 \times 10^{-3}$ as already described in Section 5.2.1. Using Fig. 20 and fixing $\alpha = 6 \times 10^{-3}$, we therefore find a maximum $\dot{M}_{\rm CO}$ of 0.3 $M_\oplus$ Myr^{-1} to still produce a best fit (at the 99.7 per cent uncertainty level) in the case when steady state is not yet reached.

We note that when higher resolution images become available, the present model should be extended to a 1D code that viscously evolves CO and carbon together, since that would allow to compare the predicted radial profiles to that observed.

5.3 Cometary composition

Using equation (1) in Kral et al. (2017c), we find that the dust production rate in this belt is ∼1.7 $M_\oplus$ Myr^{-1}, where we assumed a dr/r of ∼0.85 as derived in Section 3.2, and the fiducial values listed in Kral et al. (2017c). This in turns leads to a prediction of the CO-to-solid mass ratio of < 20 per cent using the maximum $\dot{M}_{\rm CO}$ of 0.3 $M_\oplus$ Myr^{-1} that we have just derived in the previous section (see equation 2 in Kral et al. 2017c). The upper limit we derive here is thus consistent with the largest values known for Solar System comets where the CO-to-dust mass ratio is of 3–27 per cent (Mumma & Charnley 2011).

As the CO-to-dust mass ratio is found to be consistent with Solar System comets, we can predict the amount of water that should be released together with CO. Using that $2 \times 10^{-3} < \dot{M}_{\rm CO} <$ 0.3 $M_\oplus$ Myr^{-1} and that typical H_2O-to-CO mass ratios span a large range of 3–160 (Mumma & Charnley 2011), this translates to $6 \times 10^{-3} < \dot{M}_{\rm H_2O} < 2$ $M_\oplus$ Myr^{-1} (we limit the upper bound to 2$M_\oplus$ Myr^{-1} because this rate cannot be greater than the dust mass-loss rate estimated above). The water photodissociation time-scale is very short and will not be much affected by the lack of UV photons with $\lambda < 110$ nm (see Fig. 2) because lower energy photons with $110 < \lambda < 190$ nm can still photodissociate H_2O (contrary to CO). Thus, the amount of water is expected to be small but we can derive the amount of neutral hydrogen H that should survive together with carbon and oxygen for more than the age of the system (a few viscous time-scales). Assuming that the release of CO (or that the onset of the collisional cascade) started 10 Myr ago (i.e. after the protoplanetary disc dispersed), we find that a mass $\sim 7 \times 10^{-3}$–2 $M_\oplus$ of H could be in the system.

Following a similar procedure, we also find that the total oxygen mass in the system coming from CO and H_2O photodissociations should be in the range 0.06–20 $M_\oplus$, which thus may be the dominant species in the system.[6] Even if water is not released together with CO, then the oxygen mass will still be very similar to the carbon mass (times 16/12) and so would be of order 10^{-2} $M_\oplus$. Moór et al. (2015) used Herschel to look for [OI] in HD 131835 and assuming LTE plus that the temperature is ∼30 K, they find a mass upper limit of 10^{-2} $M_\oplus$, which is similar to our estimation when oxygen only comes from CO but slightly lower than our lower mass prediction if water is released as well. However, LTE may not be a good approximation for OI (and then the oxygen upper limit could be much higher) because the critical collider density (of electrons or H) to reach LTE for OI is $\sim 3 \times 10^5$ cm^{-3}, which may be higher than predicted by our models (especially away from R_0). Indeed, in Section 4.2.2, we found that the C^0 number density could be a few 10^3 cm^{-3} but owing to the low ionization fraction, the electron density (coming from carbon photoionization) may be rather small. If water is released, the hydrogen number density could be 10–500 times higher, i.e. the exact value of the hydrogen number density is needed to determine whether LTE is reached. If LTE is not reached, it would mean that the mass upper limit from Herschel could be order of magnitude higher in non-LTE, as already shown in Kral et al. (2016). From the observations at hand, it is thus hard to put any constraints on the release of water from the planetesimals, we can only say that the OI upper limit from Herschel is consistent with a secondary origin.

[6]However, we note that the upper value of 20 $M_\oplus$ is large and in the upper range compared to the total amount of oxygen expected to be available at this stage (e.g. Kamp et al. 2011).

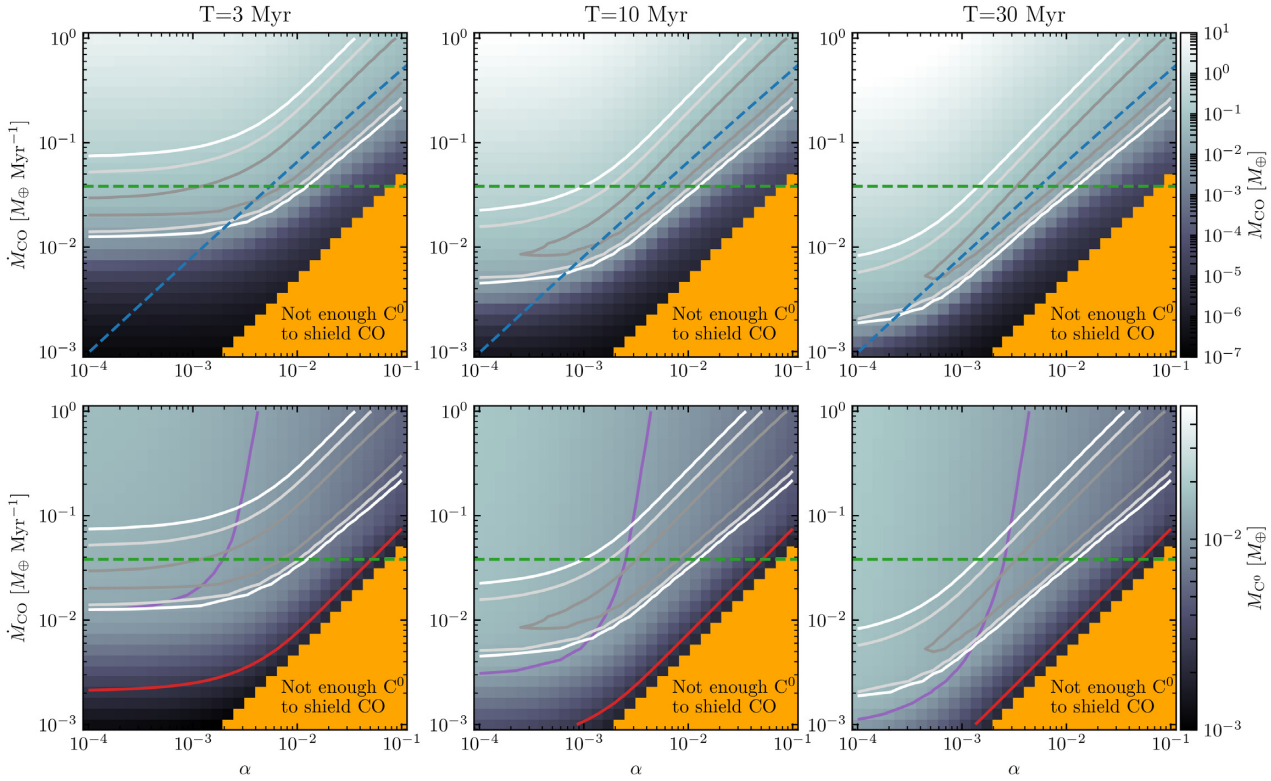

Figure 20. Best-fitting values to get $M_{CO} = 0.04$ M$_\oplus$ as observed with ALMA for HD 131835, in the parameter space $\dot{M}_{CO}$ versus α. These results are based on the model presented in Section 5.2.2. The three columns correspond to different evolution time from when the secondary production of gas has started. *Top:* The colour-scale is showing the CO mass M_{CO} and the contours are plotted for 1, 3, and 5σ from the observed value. The yellow region is where C^0 does not reach densities that are high enough to shield CO. The blue dashed line is the prediction from the analytical model presented in Section 5.2.1. The green dashed line shows the expected CO production rate $\dot{M}_{CO}$ from the stellar and disc parameters (see Matrà et al. 2017b). *Bottom:* Total C^0 mass needed to produce $M_{CO} = 0.04$ M$_\oplus$ in different parts of the parameter space. The red and purple lines are for C^0 masses of 2.7×10^{-3} and 1.2×10^{-2} M$_\oplus$ (predicted range from observations), respectively. We overlay the CO contours from the top plots to check where the best-fitting models lie in terms of C^0 masses.

5.4 Dust/gas interactions

Owing to the high-CO, carbon, and presumably oxygen content in the gas disc around HD 131835, the gas density may be high enough to drag the dust. To check that, we work out the dimensionless stopping time (Takeuchi & Artymowicz 2001)

$$T_s = 8 \left(\frac{M_\star}{1.7\,\mathrm{M}_\odot}\right)^{1/2} \left(\frac{T}{30\,\mathrm{K}}\right)^{-1/2} \left(\frac{R}{100\,\mathrm{au}}\right)^{-3/2} \times \left(\frac{\rho_s}{1500\,\mathrm{kg\,m^{-3}}}\right) \left(\frac{s}{10\,\mu\mathrm{m}}\right) \left(\frac{n_g}{10^5\,\mathrm{cm^{-3}}}\right)^{-1}, \quad (11)$$

where ρ_s is the density of the solids, s the grain size, T the gas temperature, and n_g the gas density. This equation shows that in less than 10 orbital time-scales at 100 au, a dust grain of about 10 microns would be entrained by the gas and migrate radially if its density is around 10^5 cm^{-3}. Such high densities are not inconceivable close to R_0 in the disc around HD 131835. Indeed, assuming that the CO gas disc is 0.04 M$_\oplus$ (Moór et al. 2017) and extends over $\Delta R =$ 70 au, we find that the CO number density is already $\sim 5 \times 10^3$ cm^{-3}. In Section 4.2.2, we also found that the C^0 number density could go up to a few 10^3 cm^{-3} on top of which some oxygen and hydrogen (coming from the release of water together with CO) would increase the total number density up to $>10^4$ cm^{-3}. Hence, the gas is expected to be able to exchange angular momentum with the smallest dust grains in the system, therefore potentially leading to a radial displacement of these grains from their point of origin.

The exact interplay between the effect of gas drag and collisions is complex. Collisions will prevent grains from migrating too far (due to gas drag) as they may be destroyed before reaching their new steady state position, which needs to be modelled accurately. Here, we simply suggest that this gas drag may be able to explain the presence of narrow rings as observed with SPHERE in scattered light (Feldt et al. 2017) because small micron-sized grains will accumulate at the outer edge of the gas disc where its density plummets (Takeuchi & Artymowicz 2001; the furthest B1 ring is at ~116 au, Feldt et al. 2017) and a second ring also composed of larger grains will be left at the parent belt position (the outer edge of the B2 ring is ~84 au, Feldt et al. 2017).

The increased lifetime of this small dust could also result in shielded secondary discs having on average a smaller grain size that is closer to the blow-out limit (i.e. around 2.5 μm in this system, Burns et al. 1979) than their unshielded counterparts, evidence for which is seen in Lieman-Sifry et al. (2016).

5.5 Are all hybrid discs actually shielded discs of secondary origin?

The new scenario suggested in this paper opens the possibility that all potential hybrid discs are actually shielded discs of secondary

Table 3. Table describing the disc and stellar parameters of the hybrid/shielded discs with known CO masses (calculated from optically thin CO isotopic lines).

System	R (au)	ΔR (au)	M_{CO} ($M_\oplus$)	T^a (K)	$L_{IR}/L_\star$	age (Myr)	$L_\star$ ($L_\odot$)
HD 131835 (1, 3)	90	80	0.04	30	2×10^{-3}	16	10
HD 21997 (2, 3)	70[b]	30[b]	0.06	9	6×10^{-4}	42	14
HD 121191 (4, 5)	100[c]	40[c]	3×10^{-3}	6	2×10^{-3}	15	7
HD 121617 (4)	83	60	0.02	18	5×10^{-3}	16	14
HD 131488 (4)	85	40	0.09	10	2×10^{-3}	16	12

[a]Gas temperatures are lower limits because of possible beam dilution. [b]For HD 21997, we take the planetesimal belt radius at which 70 per cent of the surface density is located as being the reference radius, and the disc half-width as being from the reference radius to the inner radius derived in (3). [c]The disc around HD 121191 was not resolved (or only marginally) in (4) and thus we use an SED fit [from (5) where we added the ALMA flux] to obtain the disc radius (and we correct from blackbody using Pawellek & Krivov 2015). For the disc width, we arbitrarily assume the same width as for HD 131488. References: (1) this paper, (2) Kóspál et al. (2013), (3) Moór et al. (2013), (4) Moór et al. (2017), (5) Kral et al. (2017c).

origin. So far, nine systems (including HD 131835) have been suggested to be hybrid, namely HD 21997, HD 138813, 49 Ceti, HD 32297, HD 156623, HD 121191, HD 121617, and HD 131488 (Kóspál et al. 2013; Greaves et al. 2016; Lieman-Sifry et al. 2016; Hughes et al. 2017; Moór et al. 2017). Out of these nine potential hybrid members, five have been detected with an optically thin CO isotope line (namely HD 131835, HD 21997, HD 121191, HD 131488, and HD 121617) and thus have accurate CO measurements (Moór et al. 2017). For these, we apply the same method as described in Section 5.2.3 to compute the range of α and C^0 mass values that can fit the observed CO masses for each system (listed in Table 3). The results are shown in Fig. 21 in a similar way to Fig. 20.

We find that the range of $\dot{M}_{CO}$ implied by the best-fitting values (contours) always overlaps with the predicted range (green dashed lines from Matrà et al. 2017b) derived for a given system. This reinforces the point that these systems could be shielded discs rather than hybrid discs. In Fig. 21 (right), we also show the potential C^0 mass that is needed to explain the observed CO. The predicted C^0 masses are all above 10^{-3} $M_\oplus$ and would be easily detectable with ALMA, which therefore have the potential to assess the secondary origin of these gas discs.

We find that HD 131835 and HD 21997 need α values lower than 10^{-2} to explain the observations, while HD 121191, HD 121617, and HD 131488 can be explained with $10^{-2} < \alpha < 1$ owing to their high CO input rate. The latter three systems are thus expected to be at steady state while the former two may still be evolving.

We conclude that all hybrid discs with accurate CO masses observed so far may be consistent with being shielded discs of secondary origin and that observations of [CI] with ALMA have the potential to confirm this possibility. The observed C^0 mass would also give insights into the most probable α value for each system and thus provide information as to what is driving the viscosity in these debris disc systems (e.g. whether this is the MRI, Kral & Latter 2016). We note, however, that this shielded/unshielded dichotomy seems to emerge because of differences both in α and $\dot{M}_{CO}$. Interestingly, the $\dot{M}_{CO}$ values for β Pic and most hybrid discs are similar but the CO content observed is orders of magnitude different. A difference in α could explain these two different regimes but our model does not address the origin of the α values. It could be that β Pic is actually still evolving towards that shielded stage (see the thin lines on Fig. 19 that are for an evolution that has started only recently). However, it could be that α can be very different from system to system depending on the ionization fraction or some other parameters that are yet to be understood.

5.6 Confirming observationally whether hybrid/shielded discs are of primordial/secondary origin

In this paper, we showed that massive CO gas discs may be well explained by secondary production of gas released from planetesimals in debris belts. However, can we rule out that the observed gas is primordial?

The main difference between a primordial and secondary gas disc is that we expect the former to be dominated by H_2 with a typical H_2-to-CO ratio of 10^4, while the latter is depleted in H_2 and dominated by CO, carbon, oxygen (and hydrogen, if water is released together with CO). This has several consequences which we comment on further below.

We find that it is too early to rule out a primordial origin for sure, even though, at the moment, the primordial origin is suggested based on the sole high gas-mass content of these discs but there are no observational/theoretical proofs to back it up. Importantly, it is still to be proven how these discs could survive against photoevaporation for >10 Myr (e.g. Owen, Clarke & Ercolano 2012)? Here, we provide some ideas for some new observations that could be used to find the real origin of the gas.

Temperature: Gas temperatures that are much lower than dust temperatures seem to be the norm for shielded/hybrid discs (e.g. Moór et al. 2017). In a protoplanetary disc such low temperatures are not expected but it remains an open question whether in a hybrid disc scenario with low dust content such temperatures could be reached. To the authors' knowledge this has not been simulated so far. Another possibility is that the measured low excitation temperature could also be due to non-LTE effects, which would mean the actual kinetic temperature is higher (e.g. Matrà et al. 2015). However, as shown in Fig. 16 (right), for a gas with a secondary origin, it is possible to reach very low kinetic temperatures. We also find (using DALI) that adding sulphur in these discs can lower the temperatures even further. The exact composition of the gas disc is thus very important to set-up the temperature but it goes beyond the scope of this paper to study this in detail. These low temperatures could be another hint that a secondary origin is more likely.

Spatial distribution of CO VS dust and VS C^0: One prediction of the model is that CO in these discs can extend further than the main planetesimal belt as it has time to spread viscously, which may explain, for instance, why the CO gas disc around HD 21997 is more extended inwards than its dust belt (Kóspál et al. 2013). Moreover, we also predict that C^0 should be colocated with CO in the inner region but not in the outer region. Indeed, CO will evolve together with C^0 only in the regions where the C^0 density is high enough

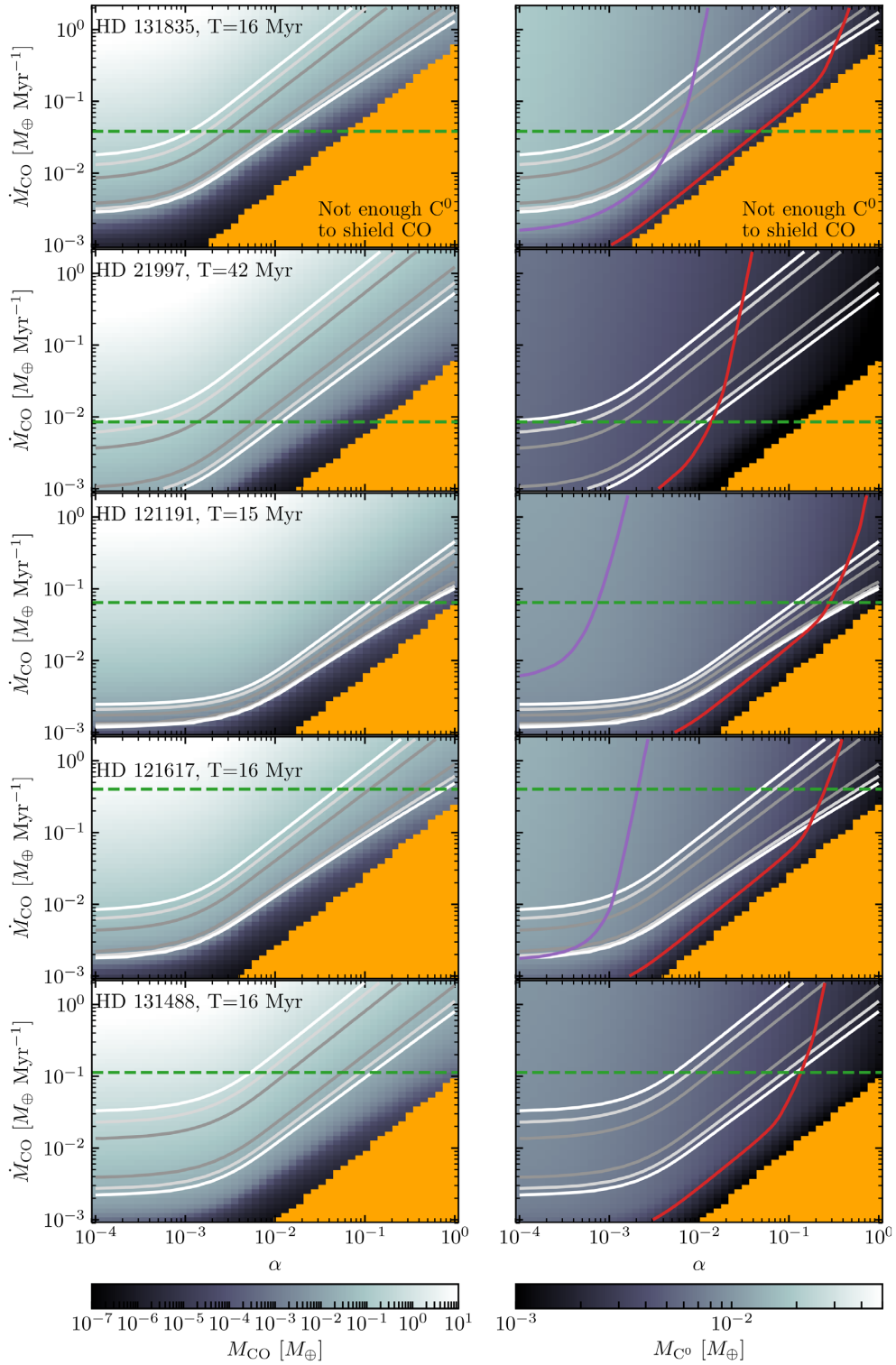

Figure 21. *Left:* Best-fitting values to get the observed $M_{\rm CO}$ as observed with ALMA for HD 131835, HD 21997, HD 121191, HD 121617, and HD 131488 (see Table 3), in the parameter space $\dot{M}_{\rm CO}$ VS α assuming that the system evolved over a time-scale close to its age. The colour-scale is showing the CO mass $M_{\rm CO}$ and the contours are 1, 3, and 5σ from the observed value. The yellow region is where C^0 does not reach densities that are high enough to shield CO. The green dashed line shows the expected CO production rate $\dot{M}_{\rm CO}$ from the stellar and disc parameters (see Matrà et al. 2017b). *Right:* Total C^0 mass needed to produce the observed $M_{\rm CO}$ values in different parts of the parameter space (the best-fitting contours for the CO mass are overplotted). The red and purple lines are for C^0 masses of 3×10^{-3} and 10^{-2} $M_\oplus$, respectively (typical range expected in shielded discs).

to shield CO beyond which the CO density would fall drastically, meaning that CO and C^0 would not be colocated in the outer region. In a protoplanetary disc, we expect an onion structure, with CO in the mid-plane and C^0 above it and thus CO and C^0 are expected to be colocated radially (though not vertically). The main observational difference between the primordial VS secondary profile is that of the steep drop of CO predicted for the secondary origin (while C^0 can extend further out) and thus we expect this non-colocation of CO and C^0 only in the secondary scenario. We note that this will happen in regions where the carbon density is smaller and deep observations may be needed to actually see the non-colocation of CO and CI. Resolving together CO and C^0 with ALMA would thus enable to test for consistency with a model in which the gas is secondary.

Scale height: We also note that from a high-resolution ALMA image of the system, one could measure the scale height of the gas disc. This scale height depends only on the mean molecular weight of the gas (as soon as we know the gas disc temperature) and we could thus directly show that the gas is secondary/primordial from such an observation. This has already been tried for 49 Ceti where Hughes et al. (2017) find some evidence that the scale height is low in this gas-rich system (hence favouring a high molecular weight and thus a secondary origin). Note that for this to work, the temperature should be known rather accurately at a specific radius where the scale height is measured. We could use the same method as described in Section 4.2 to get the temperature using data with a higher resolution or multitransitions of optically thin species such as $C^{18}O$ (e.g. Matrà et al. 2017a).

Spatial distribution of mm-dust: From such a high-resolution ALMA image, we could also study in more detail the spatial distribution of the millimetre dust. In Section 5.4, we showed that for a secondary origin, grains of tens of microns or smaller could migrate due to the gas. However, our equation (11) can also be used for a primordial origin for which the gas density would go up by orders of magnitude. Assuming an H_2-to-CO ratio of $>10^3$, we would have a gas density that can reach $\gtrsim 10^7$ (as we had found that the CO gas density from observations is $\sim 5 \times 10^3$ cm^{-3}), at which point millimetre grains would start migrating as well, which could form an enhancement of dust at a specific location in the disc (Takeuchi & Artymowicz 2001).

All of this together would help to confirm the origin of the gas in these systems.

6 SUMMARY/CONCLUSION

The most major outcome of this paper is that we present a new way to explain the so-called hybrid discs (>10 Myr old systems, which contain protoplanetary disc levels of CO gas) with a second-generation model. In this secondary approach, molecular gas is released from planetesimals which then photodissociates to create an atomic gas disc that spreads viscously. If the molecular gas input rate is high enough and/or that the produced atomic gas can accumulate for long viscous time-scales (i.e. small α values), we find that the neutral carbon mass that can accumulate is high enough to start shielding CO (see Section 2). The massive gas discs produced by this new secondary scenario are thus not hybrid discs (for which gas is supposed to be primordial) but rather *shielded discs* of secondary origin as we call them throughout the paper.

By fitting the new [CI] ALMA observation around HD 131835 (see Section 4.2), we find that the C^0 is mostly between 40 and 200 au with a mass that is $2.7 \times 10^{-3} < M_{C^0} < 1.2 \times 10^{-2}$ M$_\oplus$, which is high enough to shield CO. In Section 5.2.1, we present a simple analytical model that integrates shielding by C^0 and we compute the α value needed to get the CO mass of 0.04 M$_\oplus$ observed with ALMA towards HD 131835. We find that in order to shield CO at the right level, α should be between [2.5–60] $\times 10^{-4}$, which would create $\sim 10^{-2}$ M$_\oplus$ of C^0 in agreement with the observations.

We then refine the analytical model (see Section 5.2.2) and include self-shielding from CO as well as a time-dependence as C^0 takes time to accumulate, and we also take into account that the CO photodissociation time-scale can become longer than the viscous time-scale for shielded discs, meaning that CO will spread viscously before it has time to photodissociate. This refined model confirms our previous results and that α should be on the order of 10^{-3} to get a good fit of both CO, C^0, and the dust (as the CO input rate is set by the amount of dust in the system as more dust means more CO released). We also find that the C^0 mass required is compatible with that observed.

Finally, in Section 5.5, we show that this new shielded disc scenario could explain all massive (previously called hybrid) gas discs as being shielded discs of secondary origin. We find that the C^0 mass in these systems should be high and detectable with ALMA, which therefore has the potential to test our model further (and distinguish it from a primordial origin model, see Section 5.6) and also to constrain the viscosity in these systems, thus giving access to the possibility of studying what is the main driver of angular momentum in these discs.

From a more detailed perspective, we find that the second-generation shielded discs can have CO that is not necessary colocated with the parent belt (thus explaining resolved systems such as HD 21997). We also find that the CO density in shielded secondary discs should abruptly drop when the C^0 density drops below a certain threshold, thus giving the opportunity to distinguish from a primordial gas disc from high-resolution images of CO and CI. Another smoking-gun evidence to distinguish between primordial and secondary would be to measure the scale height of these discs (see Section 5.6).

By using a Photodissociation region (PDR)-like model, we also find that the typical low temperature of these massive CO discs can be explained in a shielded disc scenario because of the interplay between heating by carbon photoionization and cooling through the OI and CII lines.

For these massive gas discs, we also find that CN, N_2, and CH^+ will also be partially shielded by C^0 and are thus expected to be the most abundant molecular species, after CO, in these shielded discs. We note that the detection of CH^+ would lead to an estimate of the amount of hydrogen in these systems, as well as potentially the amount of water that is released from planetesimals together with CO.

We find that the total gas mass in HD 131835 may be able to drag the smallest dust grains, which may potentially explain the creation of rings similar to what observed in scattered light with SPHERE in this system. Moreover, because of the increased lifetime of small dust grains due to gas drag, we expect that shielded secondary discs should have on average a smaller grain size that is closer to the blow-out limit than their unshielded counterparts, evidence for which is seen in Lieman-Sifry et al. (2016).

ACKNOWLEDGEMENTS

This paper is dedicated to Manon. We thank the referee for a fair and insightful report. QK thanks Rik van Lieshout for insightful discussions about theoretical aspects of the gas model. QK thanks Simon

Bruderer for his help on DALI. QK and MCW acknowledge funding from STFC via the Institute of Astronomy, Cambridge Consolidated Grant. LM acknowledges support from the Smithsonian Institution as a Submillimeter Array (SMA) Fellow. This paper makes use of the following ALMA data: ADS/JAO.ALMA#2016.1.0.01253.S. ALMA is a partnership of ESO (representing its member states), NSF (USA), and NINS (Japan), together with NRC (Canada) and NSC and ASIAA (Taiwan) and KASI (Republic of Korea), in cooperation with the Republic of Chile. The Joint ALMA Observatory is operated by ESO, AUI/NRAO, and NAOJ. This work has made use of data from the European Space Agency (ESA) mission *Gaia* (https://www.cosmos.esa.int/gaia), processed by the *Gaia* Data Processing and Analysis Consortium (DPAC, https://www.cosmos.esa.int/web/gaia/dpac/consortium). Funding for the DPAC has been provided by national institutions, in particular the institutions participating in the *Gaia* Multilateral Agreement.

REFERENCES

Balbus S. A., Hawley J. F., 1998, Rev. Mod. Phys., 70, 1
Bohren C. F., Huffman D. R., 1983, Wiley, New York, p. 1983
Brandeker A. et al., 2016, A&A, 591, A27
Brinch C., Hogerheijde M. R., 2010, A&A, 523, A25
Bruderer S., 2013, A&A, 559, A46
Bruderer S., van Dishoeck E. F., Doty S. D., Herczeg G. J., 2012, A&A, 541, A91
Burns J. A., Lamy P. L., Soter S., 1979, Icarus, 40, 1
Cataldi G. et al., 2014, A&A, 563, A66
Cataldi G. et al., 2018, ApJ, 861, 72
Dohnanyi J. S., 1969, J. Geophys. Res., 74, 2531
Draine B. T., 2003, ApJ, 598, 1017
Dullemond C. P., Juhasz A., Pohl A., Sereshti F., Shetty R., Peters T., Commercon B., Flock M., 2012, Astrophysics Source Code Library, ascl:1202.015
Favre C., Cleeves L. I., Bergin E. A., Qi C., Blake G. A., 2013, ApJ, 776, L38
Feldt M. et al., 2017, A&A, 601, A7
Foreman-Mackey D., Hogg D. W., Lang D., Goodman J., 2013, PASP, 125, 306
Gaia Collaboration, 2016a, A&A, 595, A1
Gaia Collaboration, 2016b, A&A, 595, A2
Goodman J., Weare J., 2010, Commun. Appl. Math. Comput. Sci., 5, 65
Greaves J. S. et al., 2016, MNRAS, 461, 3910
Higuchi A. E. et al., 2017, ApJ, 839, L14
Hughes A. M., Wilner D. J., Andrews S. M., Williams J. P., Su K. Y. L., Murray-Clay R. A., Qi C., , 2011, ApJ, 740, 38
Hughes A. M. et al., 2017, ApJ, 839, 86
Hung L.-W., Fitzgerald M. P., Chen C. H., MIttal T., Kalas P. G., Graham J. R., 2015a, ApJ, 802, 138
Hung L.-W., 2015b, ApJ, 815, L14
Kamp I., Woitke P., Pinte C., Tilling I., Thi W.-F., Menard F., Duchene G., Augereau J.-C., 2011, A&A, 532, A85
Kóspál A. et al., 2013, ApJ, 776, 77
Kral Q., Latter H., 2016, MNRAS, 461, 1614
Kral Q., Thébault P., Charnoz S., 2013, A&A, 558, A121
Kral Q., Wyatt M., Carswell R. F., Pringle J. E., Matrà L., Juhász A., 2016, MNRAS, 461, 845
Kral Q., Clarke C., Wyatt M., 2017b, in Hans J. D., Juan A. B., eds, Handbook of Exoplanets. Springer International Publishing, p. 165
Kral Q., Matrà L., Wyatt M. C., Kennedy G. M., 2017c, MNRAS, 469, 521
Krivov A. V., Löhne T., Sremvcević M., 2006, A&A, 455, 509
Lieman-Sifry J., Hughes A. M., Carpenter J. M., Gorti U., Hales A., Flaherty K. M., 2016, ApJ, 828, 25
Löhne T., Krivov A. V., Rodmann J., 2008, ApJ, 673, 1123
Lynden-Bell D., Pringle J. E., 1974, MNRAS, 168, 603
Lyra W., Kuchner M., 2013, Nature, 499, 184
Mamajek E. E., Meyer M. R., Liebert J., 2002, AJ, 124, 1670
Marino S. et al., 2016, MNRAS, 460, 2933
Marino S. et al., 2017, MNRAS, 465, 2595
Matrà L., Panić O., Wyatt M. C., Dent W. R. F., 2015, MNRAS, 447, 3936
Matrà L. et al., 2017a, MNRAS, 464, 1415
Matrà L. et al., 2017b, ApJ, 842, 9
Matrà L., Wilner D. J., Öberg K. I., Andrews S. M., Loomis R. A., Wyatt M. C., Dent W. R. F., 2018a, ApJ, 853, 147
Matrà L., Marino S., Kennedy G. M., Wyatt M. C., Öberg K. I., Wilner D. J., 2018b, ApJ, 859, 72
Metzger B. D., Rafikov R. R., Bochkarev K. V., 2012, MNRAS, 423, 505
Moór A., Ábrahám P., Derekas A., Kiss Cs, Kiss L. L., Apai D., Grady C., Henning Th., 2006, ApJ, 644, 525
Moór A. et al., 2013, ApJ, 777, L25
Moór A. et al., 2015, ApJ, 814, 42
Moór A. et al., 2017, ApJ, 849, 123
Mumma M. J., Charnley S. B., 2011, ARA&A, 49, 471
Owen J. E., Clarke C. J., Ercolano B., 2012, MNRAS, 422, 1880
Pawellek N., Krivov A. V., 2015, MNRAS, 454, 3207
Pecaut M. J., Mamajek E. E., Bubar E. J., 2012, ApJ, 746, 154
Pringle J. E., 1981, ARA&A, 19, 137
Rafikov R. R., 2017, ApJ, 837, 163
Richert A. J. W., Lyra W., Kuchner M. J., 2018, ApJ, 856, 41
Riviere-Marichalar P. et al., 2012, A&A, 546, L8
Riviere-Marichalar P. et al., 2014, A&A, 565, A68
Rizzuto A. C., Ireland M. J., Robertson J. G., 2011, MNRAS, 416, 3108
Rollins R. P., Rawlings J. M. C., 2012, MNRAS, 427, 2328
Takeuchi T., Artymowicz P., 2001, ApJ, 557, 990
Tanaka T., 2011, MNRAS, 410, 1007
Tazzari M., Beaujean F., Testi L., 2018, MNRAS, 476, 4527
Thébault P., Augereau J.-C., 2007, A&A, 472, 169
van Dishoeck E. F. , in Millar T. J., Williams D. A., eds, Rate Coefficients in Astrochemistry, Vol. 146. Springer, Netherlands, p. 49
van Leeuwen F., 2007, A&A, 474, 653
Visser R., van Dishoeck E. F., Black J. H., 2009, A&A, 503, 323
Wyatt M. C., Smith R., Su K. Y. L., Rieke G. H., Greaves J. S., Beichman C. A., Bryden G., 2007, ApJ, 663, 365
Xie J.-W., Brandeker A., Wu Y., 2013, ApJ, 762, 114
Zuckerman B., Song I., 2012, ApJ, 758, 77

APPENDIX A: ADDITIONAL CORNER PLOT

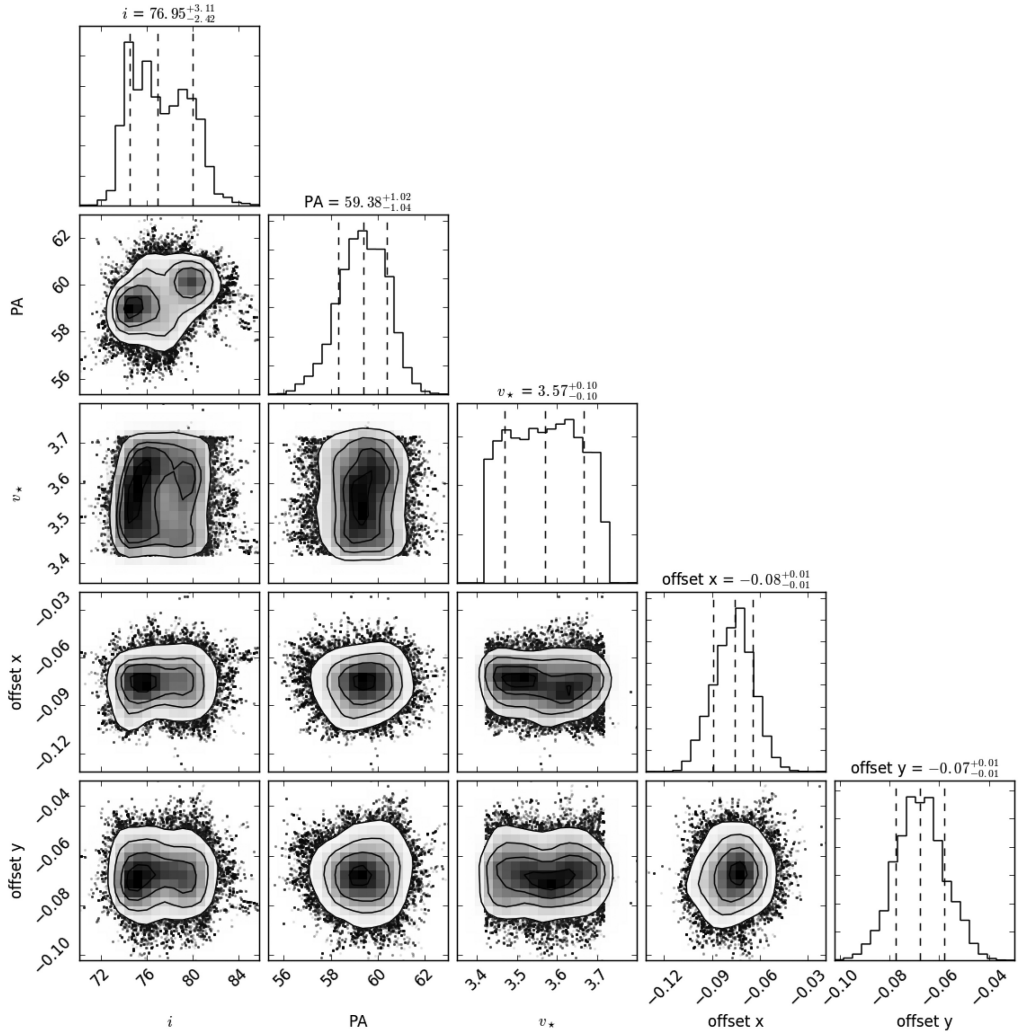

Figure A1. Posterior distribution for the gas disc for i, PA, $v_\star$, offset x and offset y (see Section 4.2). The marginalized distributions are presented in the diagonal. The vertical dashed lines represent the 16th, 50th, and 84th percentiles.

This paper has been typeset from a TEX/LATEX file prepared by the author.